Wegener Center
SCIENTIFIC REPORT
97 | 2023

Tracking global warming based on Earth energy uptake and energy imbalance modeling

Georgios Thalassinos

January 2023

Climate Change Graz
Field of Excellence
University of Graz

Wegener Center

UNI GRAZ

The Wegener Center for Climate and Global Change is an interdisciplinary, internationally recognized research and graduate education institute of the University of Graz that is pooling the University's expertise in Climate, Environmental and Global Change. It brings together research teams and scientists from fields such as geophysics and climate physics, meteorology, economics, geography, and social sciences. At the same time, close links are maintained and further developed with many national and international cooperation partners. The research interests range from monitoring, analysis, and modeling of climate and environmental change to the investigation of climate change impacts and the analysis of the human dimensions of these changes related to mitigation, adaptation, and loss & damage. More information at **www.wegcenter.at**.



Alfred Wegener (1880 – 1930), after whom the Wegener Center is named, was founding holder of the University of Graz Geophysics Chair (1924 – 1930). In his work in the fields of geophysics, meteorology, and climatology he was a brilliant scientist and scholar, thinking and acting in an interdisciplinary way, far ahead of his time with this style. The way of his ground-breaking research on continental drift is a shining role model. His sketch on the relations of continents based on traces of an ice age about 300 million years ago (left) as basis for the Wegener Center Logo is thus a continuous encouragement to explore equally innovative ways: paths emerge in that we walk them (motto of the Wegener Center).

This report is the result of a master thesis work completed in April 2022.

SR 97 | 2023 Tracking global warming based on Earth energy uptake and energy imbalance modeling
ISBN 978-3-9504700-6-2 January 2023

Suggested citation:
Thalassinos, G. (2023), Tracking global warming based on Earth energy uptake and energy imbalance modeling, Wegener Center Scientific Report 97-2023, Wegener Center Verlag, University of Graz, Austria, January 2023.
ISBN 978-3-9504700-6-2

(c) 2023 Wegener Center Verlag, University of Graz, Austria
The usage of images, tables, or texts of this Scientific Report is permitted for non-commercial purposes if appropriate credit is given.
For any other purposes, please contact: wegcenter@uni-graz.at

Publishing institution:
Wegener Center for Climate and Global Change, University of Graz
Brandhofgasse 5, 8010 Graz, www.wegcenter.at

Contact: Georgios Thalassinos
thalassinos.georg@gmail.com

Georgios Thalassinos, BSc

Tracking global warming based on Earth energy uptake and energy imbalance modeling

MASTER'S THESIS

to achieve the university degree of

Master of Science

Master's degree programme: Physics

submitted to

Graz University of Technology

Supervisor

Univ.-Prof. Dr. Gottfried Kirchengast
Wegener Center for Climate and Global Change
and Institute of Physics, University of Graz

Graz, October 2022

Abstract

Anthropogenic climate warming caused by greenhouse gas emissions has led to a positive imbalance in the energy budget of the Earth. The Earth Energy Imbalance (EEI) represents the rate of change in heat stored by the climate system in response to global warming and thus the portion of forcing the climate has not yet responded to. This study uses observations for Earth energy uptake (EEU) from 1960 to 2020 in all subsystems of the Earth system, comprising heat energy fluxes into oceans, atmosphere, land, and cryosphere. With the help of uncertainty estimates for energy uptake, EEI is assessed as a decadal-mean rate of change. The decadal-mean EEI has not only been maintained, but also increased in recent decades. Combining it with observations of effective radiative forcing (ERF) and global surface air temperature (GSAT), an energy-budget derived estimate of the climate feedback parameter of 1.4 $\mathrm{W\,m^{-2}\,K^{-1}}$ with an uncertainty of 0.4 $\mathrm{W\,m^{-2}\,K^{-1}}$ is achieved. These three variables have also been used as input parameters for a simple two-layer energy balance model used to study historical and scenario-based development of the GSAT, EEI, ERF and the climate feedback parameter. The model produced satisfactory results that agree well with observations. By using the model in alternative modes, i.e., different variables as input, it can be seen that GSAT records agree well with ERF in the decadal mean. Hope for mitigating climate warming can be drawn from using this simple model under climate change scenarios. Assuming a sustainable future, the uppermost ocean-layer component of the EEI could reach zero already near 2050. This might lead to the deeper oceans starting to act as a heat source from beneath.

Zusammenfassung

Die anthropogene Klimaerwärmung durch Treibhausgasemissionen hat zu einem Ungleichgewicht (Imbalance) im Energiehaushalt der Erde geführt. Diese Earth Energy Imbalance (EEI) stellt die Änderungsrate der Wärme dar, die vom Klimasystem als Reaktion auf die globale Erwärmung gespeichert wird, und somit den Teil, auf den das Klima noch nicht reagiert hat. Diese Studie verwendet Beobachtungen zur Earth Energy Uptake (EEU) von 1960 bis 2020 in allen Subsystemen des Erdsystems, einschließlich der Wärmeenergieflüsse in Ozeane, Atmosphäre, Land und Kryosphäre. Mithilfe von Unsicherheitsschätzungen für die Energieaufnahme wird EEI als dekadische mittlere Änderungsrate untersucht. Die dekadisch gemittelte EEI wurde in den letzten Jahrzehnten nicht nur gehalten, sondern nahm weiter zu. Kombiniert mit Beobachtungen des effektiven Strahlungsantriebs (ERF) und der globalen Oberflächenlufttemperatur (GSAT), ergibt sich eine vom Energiebudget abgeleiteten Schätzung des Klimarückkopplungsparameters von 1,4 $\mathrm{W\,m^{-2}\,K^{-1}}$ mit einer Unsicherheit von 0,4 $\mathrm{W\,m^{-2}\,K^{-1}}$. Diese drei Variablen wurden auch als Eingabeparameter für ein einfaches zweischichtiges Energiebilanzmodell verwendet, um die historische und szenariobasierte Entwicklung von GSAT, EEI, ERF und des Klimarückkopplungsparameters zu untersuchen. Das Modell lieferte zufriedenstellende Ergebnisse, die gut mit den Beobachtungen übereinstimmen. Durch die Verwendung des Modells in alternativen Modi, d. h. verschiedenen Variablen als Eingabe, ist ersichtlich, dass GSAT-Datensätze im dekadischen Mittel gut mit ERF übereinstimmen. Aus der Verwendung dieses einfachen Modells in Klimawandelszenarien kann Hoffnung auf eine Eindämmung der Klimaerwärmung geschöpft werden. Geht man von einer nachhaltigen Zukunft aus, könnte die Komponente der obersten Ozeanschicht des EEI bereits um das Jahr 2050 Null erreichen. Dies könnte dazu führen, dass die tieferen Ozeane beginnen, als Wärmequelle von unten zu fungieren.

Acknowledgements

First of all I would like to thank my supervisor Gottfried Kirchengast, who provided me with the great opportunity of a funded master thesis at the Wegener Center for Climate and Global Change. In our meetings we had the chance to dive deep into the physics of global climate change and my interest in this topic has been growing throughout the course of my work on this thesis. I am very thankful to have been given the chance to contribute so much input for various presentations and even being given the opportunity to have my results presented at a scientific conference.

I also want to thank Maximilian Gorfer, who provided a lot of the data used in this work and was always there to discuss any questions on how to incorporate results from previous work into this study.

Furthermore I would like to thank everybody from the team of the Wegener Center for Climate and Global Change, who made not only the scientific work but also the coffee breaks more interesting.

Finally, I want to thank my parents for giving me all their support in everything I always wanted to achieve and encouraging me to pursue my dreams.

Contents

1 Introduction **1**

2 Global energy budget **3**
2.1 Earth energy balance 3
2.2 Surface energy balance 5
2.3 Top-of-atmosphere radiation balance 5
2.4 Greenhouse effect 6

3 Global warming induced imbalance **7**
3.1 Perturbation of the balance equation 7
3.2 Radiative forcing 8
3.3 Radiative response 14
3.4 Earth Energy Imbalance 14
3.5 Simple Energy Imbalance modeling 16

4 Data acquisition and analysis **19**
4.1 Annual data and uncertainties 19
4.2 Decadal anthropogenic imprints 23
4.3 Decadal radiative forcing and response 26
4.4 Comparison of observational data sets 27

5 Climate feedback parameter estimation **31**
5.1 Climate sensitivity framework 33
5.2 Observational constraints 33
5.3 Time dependent evolution 34
5.4 Role of Earth Energy Imbalance 34

6 Global temperature and energy imbalance modeling **37**
6.1 Consistency with observational data 37
6.2 Probing the model under different drivers 38
6.3 Climate change scenarios up to 2050 40

7 Conclusion **43**

List of Figures **45**

List of Tables **46**

Bibliography **47**

Acronyms

AHC Atmospheric Heat Content.

CERES Clouds and the Earth's Radiant Energy System.

CEU Cryopshere Energy Uptake.

CFC chlorofluorocarbon.

CMIP6 Coupled Model Intercomparison Project Phase 6.

EEI Earth Energy Imbalance.

EEU Earth Energy Uptake.

EM electromagnetic.

ENSO El Niño–Southern Oscillation.

ERF Effective Radiative Forcing.

GHG greenhouse gas.

GSAT Global Surface Air Temperature.

IPCC International Panel on Climate Change.

LHC Land Heat Content.

LW longwave.

OHC Ocean Heat Content.

ORAS5 Ocean Reanalysis System 5.

SAOD Stratospheric Aerosol Optical Depth.

SARF Stratospheric-temperature-adjusted Radiative Forcing.

SSP Shared Socioeconomic Pathway.

SW shortwave.

TOA Top of the Atmosphere.

TSI Total Solar Irradiance.

1 Introduction

The Earth's climate is driven by incoming radiation from the Sun. This energy arrives on Earth in the form of shortwave radiation. At the upper part of our atmosphere, above the troposphere, most of the very short wavelengths are already blocked off by ozone and other gases. It is mostly the visible part of the solar spectrum that can pass the atmosphere down towards the surface. Energy conservation implies that all radiation entering the Earth system can only be transformed into other forms of energy without being lost. This principle lies at the bottom of a balanced climate, where the radiation fluxes entering the Earth system have the same magnitude as those leaving at the top of the atmosphere.

However, since the industrial revolution this balance has been perturbed, most prominently since the middle of the 20$^{\text{th}}$ century. Greenhouse gases, mainly carbon dioxide from fossil fuel combustion, have been added to the Earth's atmosphere, altering the amount of radiation being kept in the climate system and presenting itself as an imbalance.

This represents itself in the form of a measurable heat accumulation in the climate system. Studies such as Schuckmann et al. (2020) or Cheng et al. (2021) have pointed out the rising global heat content, which is the integrated amount of energy gain, in all spheres of the Earth system. Most of this heat goes into the oceans, where the heat energy travels deeper constantly. The rest of it is split into energy melting the ice caps, heating up the uppermost part of land and heating the atmosphere. The Earth Energy Imbalance (EEI) is the rate at which this energy is being accumulated over time. In a balanced climate this EEI would be zero, but currently it is observed to rise. That means not only is heat being accumulated, but the process is speeding up.

This imbalance caused by a radiative forcing of climate triggers a radiative response with rising surface and near-surface temperatures. Yet, the magnitude of the radiative response relative to temperature rise is determined by a nearly constant climate feedback parameter α_{FP} on decadal scales. This work will show a calculation of the EEI from heat uptake data sets in the time from 1960 to 2020.

In Chapter 2 an introduction into the concepts of radiative balance and the energy budget is given, also summarizing current shortcomings in the observation of these quantities.

The following Chapter 3 discusses the case of a perturbed climate as it is experienced in particular since the mid-20$^{\text{th}}$ century and introduces the terms radiative forcing and response.

In Chapter 4 datasets for all relevant quantities are presented to show the development of heat uptake and imbalance, radiative forcing and temperature rise over the last 60 years.

Chapter 5 presents the results of using the available data sets to arrive at an estimate for the climate feedback parameter and reviews theoretical arguments about this quantity.

Finally, in Chapter 6 the data were used in combination with a simple two-layer energy balance model to derive decadal climate change variables for historical data from 1960 to 2020 and by using climate change scenarios extending the results to the mid-21st century.

2 Global energy budget

Earth's climate is driven by incoming radiation from the Sun. The global energy budget is the closure of all energy fluxes in the Earth's climate system. It is driven by radiation fluxes entering and exiting the climate system.

These need to be balanced on annual to decadal scales in an equilibrium climate with no global warming or cooling. A positive imbalance causes a global warming and a negative imbalance a global cooling. The climate system has left the state of radiative balance due to increased greenhouse gas emissions (Hansen et al. 2011). Energy fluxes, measured in $\mathrm{W\,m^{-2}}$, in the following describe annual global mean values. Before focussing on the imbalance and heat storage in the climate system, the natural energy fluxes shall be discussed, that make up the natural unforced processes of Earth's climate.

Incoming solar radiation is the largest term in the energy budget. In order to maintain equilibrium the energy flux exiting the climate system must be equal to the one entering in the form of solar radiation. The focus of this work is, however, the small residual imbalance that is the net flux of energy into the climate system, i.e., not exiting at the top of the atmosphere.

Radiant energy is transported in the form of electromagnetic (EM) radiation. The electromagnetic spectrum is the range of all wavelengths that contribute to electromagnetic radiation. These range from gamma rays with very short wavelengths of $O(1\ \mathrm{pm})$ to radio waves with wavelengths of $O(1\ \mathrm{km})$. For climate science the most important parts of the spectrum are the visible (light) and infrared (thermal) radiation bands.

2.1 Earth energy balance

Sunlight arrives at the Top of the Atmosphere (TOA) as shortwave (SW) radiation at wavelengths of around 500 nm, i.e, in the visible part of the EM spectrum. It has an irradiance of about 1360 $\mathrm{W\,m^{-2}}$, also termed solar constant S_0. On annual scales it can be assumed near-constant, but on longer timescales its' natural variability is correlated primarily to the 11-year sunspot cycles and the Milankovich cycles, which will will be briefly discussed in Section 3.2 and cause small natural forcings of the climate.

Assuming Earth as a spherical black body illuminated by sunlight with no atmosphere, it is possible to construct a zero-dimensional energy balance model. In this simple picture maintaining radiative equilibrium requires total outgoing longwave radiation power ($P_{LW_{out}}$) to be equal to the incoming SW radiation power

($P_{SW_{in}}$). The balance equation for this global-mean, annual-mean equilibrium case is:

$$\begin{aligned} P_{SW_{in}} &= P_{LW_{out}} \\ S_0(1-A)\pi R_E^2 &= 4\pi R_E^2 \sigma T_e^4 \\ \frac{S_0}{4}(1-\alpha) &= \sigma T_e^4 \end{aligned} \tag{2.1}$$

The left-hand side is the sunlit area πR_E^2, where $R_E = 6371$ km is the Earth's mean radius, multiplied by the intensity of the incoming radiation S_0 and the fraction of absorbed sunlight $1 - A$, using the albedo A of Earth. The albedo is the fraction of sunlight that is directly reflected back to space by the surface and by clouds and aerosols in the atmosphere.

On the right side outgoing longwave (LW) radiation is given in terms of the Stefan-Boltzmann Law, which states that a black body at a given temperature radiates with an intensity proportional to the product of the fourth power of temperature and the Stefan-Boltzmann constant $\sigma = 5.67 * 10^{-8}$ W m^{-2}, over the global surface area $4\pi R_E^2$. The temperature in this formulation is, however, an effective temperature T_e and not the actual surface temperature of Earth and the area is that of a spherical Earth, giving rise to the factor 1/4. This shows that due to the spherical geometry each square metre on Earth's surface recieves only 340 W m^{-2} of solar radiation. Inserting an albedo $A = 0.3$, the equilibrium temperature becomes -18 °C. This would approximately be the temperature on a planet with no atmosphere. The natural greenhouse effect, however, keeps our planet at a bearable temperature of about 14 °C (approximately the 1961-1990 average), by trapping a large part of thermal radiation in the atmosphere. In the zero-dimensional model this can be approximated by an effective emissivity factor of $\tau = 0.61$ acccounting for the LW transmissivity induced by greenhouse gases, yielding a modified form of the above equation, now specified for the surface temperature T_s:

$$\frac{S_0}{4}(1-\alpha) = \tau\sigma T_s^4 \tag{2.2}$$

In a more realistic radiation transport picture, Earth has an atmosphere consisting of a sequence of thin layers, that each emit thermal radiation upwards and downwards. The Earth's atmosphere is fairly opaque to infrared LW and almost transparent to SW radiation. Due to the greenhouse gases (GHGs) that get excited at wavelengths of around 10 μm the LW radiation Earth emits from its surface is almost entirely radiated back by the atmosphere. This makes it meaningful to consider the energy balance split into fluxes at the TOA and fluxes at the surface.

2.2 Surface energy balance

Wild et al. (2014) gives estimates for the energy fluxes at the surface. From the incoming solar flux the atmosphere absorbs 79 $\mathrm{W\,m^{-2}}$ leaving 185 $\mathrm{W\,m^{-2}}$ to reach the surface. From these, the Earth's surface directly reflects 24 $\mathrm{W\,m^{-2}}$ and finally 161 $\mathrm{W\,m^{-2}}$ are absorbed by it. The SW budget is, however, not balanced. At the surface, the radiation heats land and oceans converting the energy into sensible and latent heat as well as thermal radiation. Wild et al. (2014) gives a value of 397 $\mathrm{W\,m^{-2}}$ for upwards thermal radiation from the surface. This is almost entirely compensated for by the 342 $\mathrm{W\,m^{-2}}$ radiated back by the atmosphere due to its greenhouse gas content. The residual of the upward flux passes thorugh the atmospheric window (specific wavelength band 10 μm) directly into space. In these specific wavelength bands of the EM spectrum neither water vapor nor other GHGs except some chlorofluorocarbons (CFCs) are active.

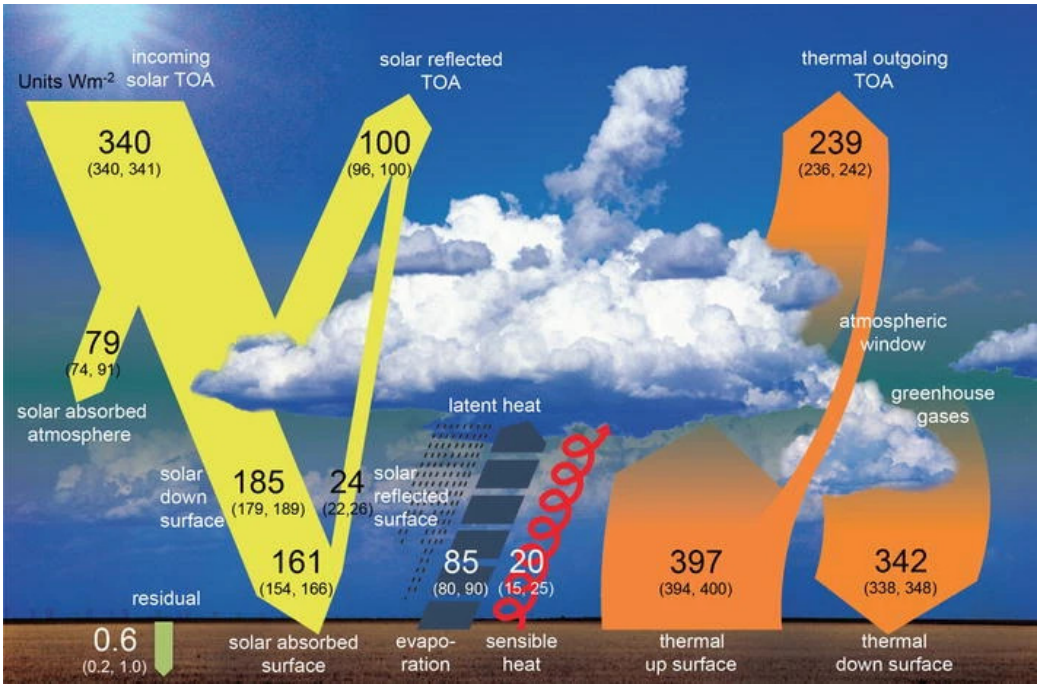


Figure 2.1: The global energy budget as presented in Wild et al. (2014)

2.3 Top-of-atmosphere radiation balance

The fluxes at the Top of the Atmosphere (TOA) are well determined in the last decades since they can be measured directly by satellite instruments without knowledge about atmospheric conditions. The largest contribution here is, as stated before, the incoming solar radiation at 340 $\mathrm{W\,m^{-2}}$. It is followed by outgoing

thermal LW radiation at 239 W m^{-2} and finally reflected SW, which amounts for 100 W m^{-2}. What is missing here, is what flows into the climate system and is accumulated as energy storage. This residual flux is the Earth Energy Imbalance (EEI). With the values before one might assume that it is equal to 1 W m^{-2}, but actually these are rounded values and it stands at 0.6 W m^{-2} following Wild et al. (2014). This already points out accurate measurements as one of the great challenges in observing it. The instruments used to measure TOA fluxes would have to be very accurate to derive an absolute estimate of EEI.

In the last years the Clouds and the Earth's Radiant Energy System (CERES) experiment has achieved great progress in this field (Loeb et al. 2021). This study will show, that EEI has been varying over the last decades by using other data as a proxy. Schuckmann et al. (2020) estimated an EEI of 0.47±0.1 W m^{-2} for the period 1971-2018 and 0.87±0.12 W m^{-2} for 2010-2018, indicating an increase in the imbalance. That means the rate at which Earth is heating up is accelerating. This acceleration is due to the anthropogenic greenhouse effect.

2.4 Greenhouse effect

In the LW radiation budget there is a vertical cycling of LW radiation in the atmosphere. Certain gases that are contained in the atmosphere are called greenhouse gases (GHGs), which are the ones responsible for this process. These gases have a polar bond that leads to vibrations at the wavelengths of below and above 10 μm in the infrared part of the EM spectrum. This infrared activity allows GHGs to absorb thermal radiation, mostly from below, and radiate back in all directions.

The greenhouse effect in our atmosphere therefore naturally alters the temperature of the Earth's surface by about 32 K. Rearranging Equation (2.1) and Equation (2.2) shows that the addition of a transmissivity factor $\tau = 0.61$ for an IR-opaque atmosphere yields a difference of 147 W m^{-2} to the no-atmosphere case in Equation (2.1). This can be considered the additional radiation caused by the greenhouse effect,

$$G = \sigma T_s^4 - \sigma T_e^4 = 147 \text{ W m}^{-2}. \tag{2.3}$$

However, this is not causing the specific climatic changes of the past decades. The latter anthropogenic greenhouse effect will be discussed in the next chapter. G as formulated here represents the natural and vital greenhouse effect on Earth, that maintains Earth's temperature at the level that our current biosphere and anthroposphere have accustomed to in the ongoing Holocene period (Steffen et al. 2015).

3 Global warming induced imbalance

The emissions of greenhouse gases from fossil fuel combustion have given rise to changes in the described framework of balanced energy fluxes. They have caused an imbalance at the TOA between incoming SW and outgoing LW radiation. This imbalance continues adding heat to the climate. The rise in GHG concentrations has been too fast for climate to keep up and therefore energy is being trapped in the climate system until a new equilibrium will be reached. In the following natural and anthropogenic causes of an imbalance at the TOA will be discussed.

3.1 Perturbation of the balance equation

The Earth's precession and obliquity cause a 100 000 year timescale variability of incoming sunlight connected to the periodicity of Glacial periods. These are the Milankovich cycles. In the historical period of meteorological records a variability of 0.1 $\mathrm{W\,m^{-2}}$ in the solar radiative flux is measured due to the 11-year sunspot cycles. Apart from episodic volcanic eruptions it is the only natural climate forcer. These natural processes are, however mean-zero. Since the 1970s the climate change induced imbalance has become increasingly dominant and distinguishable from natural variations. It is not only varying but its magnitude is rising. The framework from the previous chapter can be extended to include an equilibrium apart from the natural greenhouse effect in the equations below. By expressing energy in the atmosphere as E_A the total energy in the climate system is

$$N = \frac{S_0}{4}(1 - A) - \tau\sigma T_s^4 = \frac{S_0}{4}(1 - \alpha) - E_A \tag{3.1}$$

By applying a small perturbation to this equation (first-order perturbation approach) one gets the following, which represents the deviations of the quantities from equilibrium conditions

$$\Delta N = \frac{\Delta S_0}{4}(1 - \Delta A) - \Delta E_A \tag{3.2}$$

It has to be kept in mind, however, that A and E_A are functions of various variables such as atmospheric composition, temperature, aerosol loading or land use. That means a perturbation of A and E_A will, to first order, give rise to terms that are products including the surface air temperature anomaly (ΔT_s).

In the International Panel on Climate Change (IPCC) formulation, following common convention, the way of denoting this is writing the terms that are multiplied by the surafce temperature change ΔT_s together and terms that do not contain

this quantity separately. The latter are generally termed effective radiative forcing (ΔF_e), the former radiative response, with the full imbalance equation written as follows (Forster et al. 2021):

$$\Delta N = \Delta F_e - |\alpha_{FP}| \cdot \Delta T_s. \tag{3.3}$$

If the difference ΔN between effective radiative forcing ΔF_e and surface-temperature-related radiative response is different from zero the climate system undergoes a climatic change. Per definition a positive net imbalance ΔN with $\Delta F_e > |\alpha_{FP}| \cdot \Delta T_s$ means global warming and a negative imbalance would correspond to cooling.

ΔF_e represents the sum of all relevant natural and anthropogenic forcings, that are further discussed in Section 3.2 below. α_{FP} represents the climate feedback parameter, which is given in W m^{-2} K^{-1}. It is a measure of the radiative response of the climate system per unit surface-temperature change, composed of the sum (negative by convention) of all feedback variables f_i that have a direct effect on the TOA imbalance.

$$\alpha_{FP} = -\sum_i \frac{\partial N}{\partial f_i} \frac{\mathrm{d}f_i}{\mathrm{d}T}. \tag{3.4}$$

The imbalance equation Equation (3.3) is formulated in usual practice to correspond to a Top of the Atmosphere (TOA) at Earth's tropopause level, where most of the airmass is situated and radiation transport occurs below. So-called stratospheric adjustments account for small corrections against the actual top of the Earth's atmosphere (Forster et al. 2021).

3.2 Radiative forcing

First, it is important to know how much energy is added by external climate forcings through the forcing ΔF_e, termed Effective Radiative Forcing (ERF) hereafter. This is the globally averaged driving force in the climate, resulting from changes in the Earth system since the preindustrial period. It consists of anthropogenic and natural climate forcings. Every change in a specific climate variable presents itself as an energy flux potentially adding to climate warming. In most climate-relevant applications, the focus lies on anthropogenic radiative forcings. Before coming to these further below, the major natural climate forcings are outlined.

Natural forcings

As stated in the previous chapters the Sun provides SW radiation to the Earth. The magnitude of the flux, however, varies on timescales of the 11-year sunspot cycle. This solar forcing lies in the range of ± 0.1 W m^{-2}. In this study observations of solar forcing from three different sources have been taken into consideration.

All of these provide Total Solar Irradiance (TSI) in $\mathrm{W\,m^{-2}}$. The related effective radiative forcing component is then computed via

$$\Delta F_{solar} = \Delta\mathrm{TSI} \cdot (\Delta T_{trop} + \Delta T_{strat}) \frac{1-A}{4} = \Delta\mathrm{TSI} \cdot 0.72 \cdot \frac{1-A}{4}. \tag{3.5}$$

Smith et al. (2021a) gives a value of 0.29 for the albedo A, yielding $\Delta F_{solar} = \Delta\mathrm{TSI} \cdot 0.72 \cdot 0.71/4$ for ERF from solar forcing variability.

For the other natural part of the radiative forcing, which is volcanic, the calculation requires knowledge of the Stratospheric Aerosol Optical Depth (SAOD). In explosive volcanic eruptions large amounts of SO_2 forming reflective stratospheric aerosols are added to the atmosphere. This causes a negative contribution to the ERF, because less solar radiation can pass through the stratosphere to reach the surface of Earth. Despite its large effect of up to $-1.8\ \mathrm{W\,m^{-2}}$ for the eruption of Mt Pinatubo in 1992, volcanic radiative forcing is episodic and the aerosols remain in the stratosphere only on timescales of up to a year. To derive $\mathrm{ERF_{vol}}$, the dimensionless SAOD is multplied by an empirically determined scaling factor of $-20\ \mathrm{W\,m^{-2}}$ (Larson and Portmann 2016),

$$\Delta F_{vol} = -20 \cdot \mathrm{SAOD}. \tag{3.6}$$

Greenhouse gas forcing

In addition to the natural forcings there are also anthropogenic forcing components, that have been increasing since industrialization has started. The most prominent of these is the forcing due to carbon dioxide. Its atmospheric lifetime gives rise to a very long climate warming effect. Naturally carbon dioxide (CO_2) levels have always risen in the past, but the rate of change in CO_2 emissions in the current time is unprecedented.

In order to calculate the radiative effect of rising CO_2 levels, the global mean mole fraction of CO_2 (C) and nitrous oxide (N_2O, N) is required. From these the Stratospheric-temperature-adjusted Radiative Forcing (SARF) or ΔF^s can be calculated using the formulae by Meinshausen et al. 2020. The second most important well-mixed greenhouse gas after CO_2 is methane (CH_4). Its concentration M has an effect on ERF by N_2O as well.

Before calculating SARF the maximal range $C_{\alpha_{\max}}$ of these equations is derived by

$$C_{\alpha_{\max}} = C_0 - \frac{b_1}{2a_1} \approx 1808\ \mathrm{ppm}. \tag{3.7}$$

The preindustrial concentration of carbon dioxide C_0 and the two constants a_1 and b_1 are given in Table 3.1.

Although current CO_2 levels are far from this, it needs to be adressed for climate change scenarios incorporating higher carbon dioxide concentrations. The SARF of carbon dioxide below this level is calculated by

$$\Delta F^s_{\mathrm{CO_2}} = (\alpha' + \alpha_{\mathrm{N_2O}}) \cdot \ln(\frac{C}{C_0}). \tag{3.8}$$

The constant α' depends on the range of concentrations and is defined as

$$\alpha' = \begin{cases} d_1 - \frac{b_1^2}{4a_1} & , C > C_{\alpha_{\max}} \\ d_1 + a_1(C - C_0)^2 + b_1(C - C_0) & , C_0 < C < C_{\alpha_{\max}} \\ d_1 & , C < C_0 \end{cases} \tag{3.9}$$

$\alpha_{\mathrm{N_2O}}$ is derived from the N_2O concentration N via

$$\alpha_{\mathrm{N_2O}} = c_1 \cdot \sqrt{N}. \tag{3.10}$$

In this manner the forcing resulting from CO_2 accounts for the absorption band overlap between CO_2 and N_2O.

SARF of methane can be derived using methane and nitrous oxide concentrations M and N together with three constants and the preindustrial methane concentration M_0.

$$\Delta F^s_{\mathrm{CH_4}} = (a_3\sqrt{M} + b_3\sqrt{N} + d_3) \cdot (\sqrt{M} - \sqrt{M_0}) \tag{3.11}$$

For nitrous oxide the expression uses M_0 and four further constants. The concentrations C and M are included to account for the overlap in absorption bands of methane and carbon dioxide with the N_2O absorption spectrum.

$$\Delta F^s_{\mathrm{N_2O}} = (a_2\sqrt{C} + b_2\sqrt{N} + c_2\sqrt{M} + d_2) \cdot (\sqrt{N} - \sqrt{N_0}) \tag{3.12}$$

The parameters used in the above equations are summarized in Table 3.1.

Although CO_2, CH_4, and N_2O have the longest absolute effect on global climate due to their large concentrations there are other GHGs that are even more efficient in warming our atmosphere on a per molecule basis. These are the synthetic CFCs. CFC-11 and CFC-12 have about 10 000 times more radiative efficiency (in $\mathrm{W\,m^{-2}\,ppb^{-1}}$) than CO_2. CFC-11 has the chemical formula CCl_3F and therefore is like CCl_2F_2 (CFC-12) is a chlorofluorocarbon. They are not only harmful for the ozone layer due to chemical interactions that deplete ozone but also very efficient greenhouse gases. Their SARF is calculated by taking the difference between their preindustrial concentration and the current level and multiplying by their radiative efficiencies. Since no natural process produces CFCs preindustrial levels (X_0) are zero. (Meinshausen et al. 2020)

$$\Delta F^s_{\text{CFC-11}} = 0.259 \cdot (X_{\text{CFC-11}} - X_0) \tag{3.13}$$

$$\Delta F^s_{\text{CFC-12}} = 0.32 \cdot (X_{\text{CFC-12}} - X_0) \tag{3.14}$$

Table 3.1: Parameters for calculating ERF of major GHGs (from Meinshausen et al. 2020)

Parameter	Value	Unit
C_0	277.15	ppm
a_1	-2.4785×10^{-7}	$\mathrm{Wm^{-2}\ ppm^{-2}}$
b_1	7.5906×10^{-4}	$\mathrm{Wm^{-2}\ ppm^{-1}}$
c_1	-2.1492×10^{-3}	$\mathrm{Wm^{-2}\ ppb^{-\frac{1}{2}}}$
d_1	5.2488	$\mathrm{Wm^{-2}}$
M_0	731.41	ppb
a_3	-8.9603×10^{-5}	$\mathrm{Wm^{-2}\ ppb^{-1}}$
b_3	-1.2462×10^{-4}	$\mathrm{Wm^{-2}\ ppb^{-1}}$
d_3	0.045194	$\mathrm{Wm^{-2}\ ppb^{-\frac{1}{2}}}$
N_0	273.87	ppb
a_2	-3.4197×10^{-4}	$\mathrm{Wm^{-2}\ ppm^{-1}}$
b_2	2.5455×10^{-4}	$\mathrm{Wm^{-2}\ ppb^{-1}}$
c_2	-2.4357×10^{-4}	$\mathrm{Wm^{-2}\ ppb^{-1}}$
d_2	0.12173	$\mathrm{Wm^{-2}\ ppb^{-\frac{1}{2}}}$

ERF is defined as SARF followed by the tropospheric temperature adjustments. Therefore SARF needs to be multiplied by a factor accounting for this adjustment. Following Meinshausen et al. (2020) these are as follows:

$$\begin{aligned} \Delta F_{\mathrm{CO_2}} &= 1.05 \cdot \Delta F^s_{\mathrm{CO_2}} & \Delta F_{\text{CFC-11}} &= 1.13 \cdot \Delta F^s_{\text{CFC-11}} \\ \Delta F_{\mathrm{CH_4}} &= 0.86 \cdot \Delta F_{\mathrm{CH_4}} & \Delta F_{\text{CFC-12}} &= 1.12 \cdot \Delta F^s_{\text{CFC-12}} \\ \Delta F_{\mathrm{N_2O}} &= 1.07 \cdot \Delta F^s_{\mathrm{N_2O}} \end{aligned} \tag{3.15}$$

Aerosol forcing

The only anthropogenic forcing term that cools the planet is aerosol forcing. Aerosols are small liquid or solid particles in the atmosphere, that either scatter or absorb radiation. They also play an important role in the formation of clouds and therefore have a great impact on small scale effects in the atmosphere. Scattering and absorption together are described as aerosol-radiation interaction (ari), whereas the effects of aerosols on clouds are denoted aerosol-cloud interaction (aci).

There are different kinds of aerosols with a variety of chemical compositions. Natural aerosols include ash from volcanic eruptions, sea spray, sand or black carbon resulting from wildfires. Anthropogenic sources are the agricultural sector and e.g. cement production but also fuel and biomass combustion. In the air all of these particles experience a series of micophysical effects adding to their heterogeneity. Aerosols have residence times of only a few days in the troposphere and their distribution is spatially and temporally strongly dependent on external factors, primarily wind. Large aerosol concentrations can usually be detected in

or close to cities and industrial areas, from where atmospheric flow can transport them up to around 2000 km.

The most evident effect of aerosols on the global radiation budget is scattering and absorption, observed as haze, dust or smoke. Absorbing aerosols also change the profiles of water vapour and temperature as well as cloud formation conditions. Bright aerosols increase the scattered radiation and therefore the albedo of a dark surface underneath, but above bright surfaces their effect becomes smaller. Conversely, dark aerosols, that absorb radiation can decrease the scattered radiation over a respective brighter surface or cloud. The majority of natural and anthropogenic aerosols increase the scattered radiation. However, aerosols from agriculture and forest fires are decreasing the radiative flux to space from clouds beneath them. (Bellouin et al. 2020)

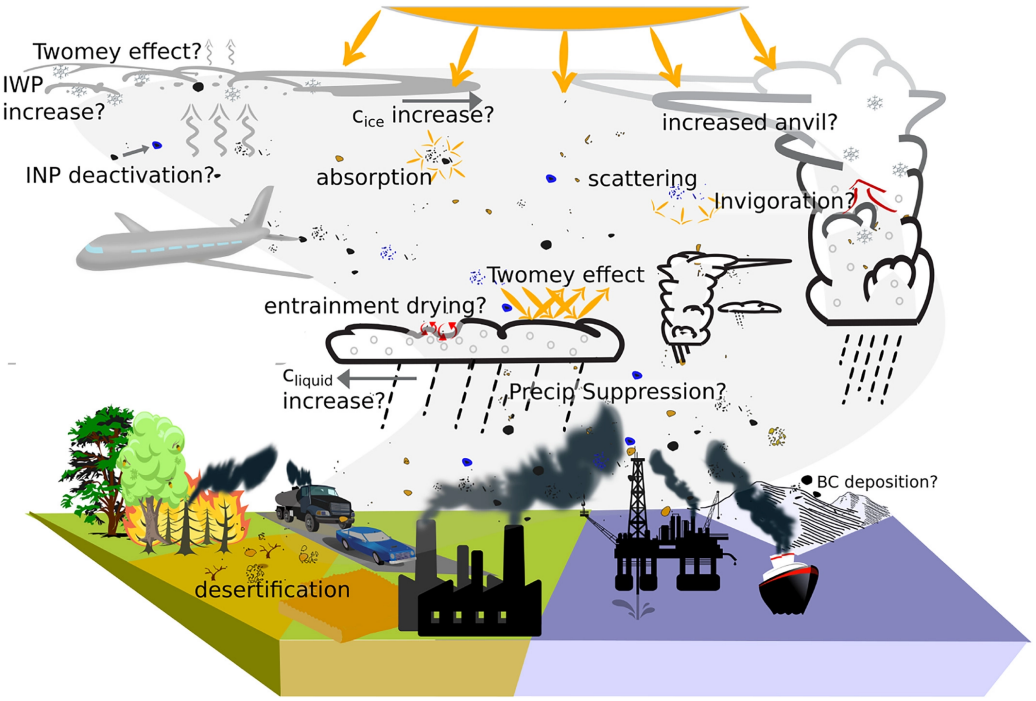


Figure 3.1: Effects of anthropogenic aerosols on the energy budget including aerosol-cloud and aerosol-radiation interactions (Bellouin et al. 2020), adapted.

The more diverse part of ERF_{aer} is the effects aerosols exert on clouds. An increase in aerosols means an increase in cloud condensation nuclei that are responsible for the formation of liquid clouds. The more droplets there are in a cloud the more radiation is reflected from the cloud-top. The cloud becomes brighter. This effect was first described by Twomey (1977). Some aerosols can also act as ice nucleating particles in ice clouds. Increase in aerosol concentration further cause delayed precipitation as well as changes in cloud thickness.

Aerosol forcing offsets the greenhouse forcing to a certain degree but is very difficult to assess exactly. There are a series of factors influencing ERF_{aer} like wavelength, incident radiation, humidity or the reflectivity of the surface for radiation interactions, whereas for cloud interactions the solubility, and chemical properties can matter as well as to whether the particles can act as cloud condensation nuclei or ice nucleating particles. Bellouin et al. (2020) still describe ERF_{aer} as the most uncertain forcing term.

It has only been since the satellite era that observations of aerosols have become available. Before this time only climate models can give an insight on the magintude of aerosol cooling. Smith et al. (2021b) used the model outputs by the most recent class of global climate models participating in the Coupled Model Intercomparison Project Phase 6 (CMIP6) to assess a time series of aerosol forcing for the industrial period. This data has been used in this study to account for aerosol cooling. Smith et al. (2021b) also showed the derived time series to be consistent with the energy uptake presented in Schuckmann et al. (2020), also partly used in this study.

Other anthropogenic forcings

There are a number of additional smaller effects that perturb the global radiation budget. In this study these terms include ozone forcing, land use change, the effects of black carbon on snow, contrails and stratospheric water vapour.

Ozone is the fourth most important greenhouse gas behind CO_2, CH_4 and N_2O, though, it is not a well-mixed greenhouse gas and therefore affects the climate on shorter timescales.

Its residence time is only about 23 days (Skeie et al. 2020). O_3 adds to the total ERF through a positive tropospheric ozone forcing and a slightly negative stratospheric component following from chemical interactions. The short residence time makes observations of the forcing difficult since spatially well-resolved data is key to assessing ozone ERF. Tropospheric ozone, which is more volatile to anthropogenic influences, has increased since the preindustrial era (Skeie et al. 2020) due to the emissions of methane, nitrous oxides, carbon monoxide and volatile organic compounds that are found in chemicals such as paint.

Stratospheric ozone has decreased due to ozone depleting substances in the last century. The most widely known of these are CFCs, which have been decreasing since the Montreal Protocol came into power regulating their emissions. This means that the ozone cooling effect on the surface from stratospheric O_3 depletion is slowly becoming smaller but the tropospheric ozone, which is adding to climate warming has been increasing lately.

Land use change affects mainly the albedo. By changing the color of land surfaces to become darker the absorbed radiation is increased and leads to warming. The same applies to black carbon on snow which makes snow-covered bright surfaces darker leading to increased absorption of radiation. Contrails from aviation also have a positive effect on ERF, since the aviation-induced cirrus clouds lead to an increase in downward thermal radiation (Lee et al. 2021). Finally, stratospheric

water vapour is proportional to methane through chemical processes and therefore follows the positive effect of methane forcing.

3.3 Radiative response

In response to a positive radiative forcing the climate system emits additional radiation to space. This response is driven by temperature rise on and near the surface as experienced in the recent times. This additional radiation tries to sustain the TOA-balanced state of the climate by increasing the surface and lower atmospheric temperatures. It, hence, acts as a counterpart to the radiative forcing. In Equation (3.3) this is expressed as the product $|\alpha_{FP}| \cdot \Delta T_s$.

This radiative response can therefore be quantified by looking at global temperature anomalies multplied by a global feedback parameter α_{FP}. While estimates of global temperature change are constrained very well, the uncertainty in α_{FP} remains large. This arises because a number of component feedbacks are included in the response that all act together in response to the forcing. Certain feedbacks might lead to effects enhancing the temperature rise, while others counteract it. A most-recent assessment from multiple lines of evidence by Sherwood et al. (2020) gives -1.30 ± 0.44 W m^2 K^{-1} as their best estimate for the total feedback parameter α_{FP}. Temperature anomalies have accuracies of about 0.05 K on a global mean basis. However, since α_{FP} is a constant it determines the overall strength of the radiative response.

3.4 Earth Energy Imbalance

The difference arising between ERF and radiative response, termed Earth Energy Imbalance (EEI, ΔN in Equation (3.3)), is the focus of this work. It arises because the rise in ERF is too fast for the radiative response to keep climate in transient equilibrium.

Inferring the imbalance as a residual of all radiation terms from Figure 2.1 is not possible due to the large uncertainties in other terms of the global energy budget (Wild 2017), that are larger than the EEI itself. However, there are other methods that can be used. These include direct radiation measurements at the TOA by satellites, more accurate measurent of energy fluxes at the Earth's surface, rates of change in heat uptake by all components of the climate system and simulations from climate models.

From these methods only two have shown to be realizable up to the desired accuracy. Since 2000 the satellite CERES is conducting accurate measurements of radiation at the TOA, allowing to determine EEI as the difference between SW and LW fluxes at the TOA by calibrating it with ocean data. Radiation measurements at the TOA as well as ocean heat content observations suggest that the global radiation budget is out of balance (Loeb et al. 2021) and the imbalance is rising.

However, extending the record back in time requires knowledge of the heat uptake by the contributors to the EEI: oceans, land, cryosphere, and atmosphere.

Schuckmann et al. (2020) achieved this by composing the most accurate data available for Ocean Heat Content (OHC), Land Heat Content (LHC), Cryopshere Energy Uptake (CEU) and Atmospheric Heat Content (AHC). These data together make up the total Earth Energy Uptake (EEU), which is the integrated imbalance over a certain timespan. Anomalies of the heat contents show the accumulated heat in each component since the reference time period. Schuckmann et al. (2020) showed an EEU of 358±37 ZJ over 1971 to 2018.

Heat content is calculated as the vertically and horizontally integrated heat energy contained in each component of the Earth system. For OHC, knowledge about sub-surface ocean temperatures $T(z)$ and sewater density $\rho(z)$ are required. To derive the OHC between two depths z_d and z_u an integral is performed over the depth z.

$$\mathrm{OHC}_{z_d - z_u} = c_w \int_{z_d}^{z_u} \rho(z) T(z) \mathrm{d}z \tag{3.16}$$

The integral is then multiplied by the seawater specific heat capacity c_w.

AHC calculation requires knowledge of sensible heat energy and latent heat energy (the heat that is released in phase transitions of water throughout the atmosphere), while kinetic energy is negligible. The integrated AHC between surface and TOA can be formulated as (Schuckmann et al. 2020; Gorfer 2022),

$$\mathrm{AHC} = \int_{z_s}^{z_{\mathrm{TOA}}} \rho \left(c_v T + g(z - z_s) + Lq \right) \mathrm{d}z. \tag{3.17}$$

In Equation (3.17) c_v describes the specific heat capacity of air, T is the air temperature, their product being the internal heat of air. The gravitational potential energy is accounted for as $g(z - z_s)$. Latent heat energy is the product of the latent heat L, based on the temperature, and specific humidity of moist air q.

LHC can be estimated from borehole climatologies, by measuring borehole temperature deviations below the surface of Earth at depths of up to 500 m. Further knowledge about the volumetric heat capacity and soil types allows to calculate LHC in a similar manner to OHC and AHC, i.e. as a vertical integral over temperature. Using 1079 logs of borehole temperature to achieve a global estimate, Cuesta-Valero et al. (2021) derived a heat accumulation of 20 ZJ from 1960 to 2018.

Although the CEU contributes a small part to the overall heat gain in the climate system its magnitude can be estimated quite well. The majority of heat flowing into the cryosphere is used to melt ice sheets, sea ice and glaciers. Thawing permafrost and snow cover reduction are not relevant on the global level. The amount of melting ice has been assessed via the mass balance of the ice caps over Greenland and Antarctica by Slater et al. (2021). Glacier contribution is estimated

from satellite gravimetry and in-situ measurements. Total CEU stands at 15 ZJ in 2018 according to Schuckmann et al. (2020).

In order to calculate decadal-average EEI timeseries, to focus on the transient climatic change information, a centered ordinary least-squares fit is applied to every eleven-year interval of EEU measurements. Its slope is the decadal EEI allocated to the respective center-year.

3.5 Simple Energy Imbalance modeling

Running large climate models to study long-term effects under different scenarios is sometimes not as effective as using so-called emulators or simple climate models. The most used in the recent IPCC context (Smith et al. 2021a; Forster et al. 2021; Gulev et al. 2021) is the two-layer energy balance model originally introduced by Geoffroy et al. (2013a) and Geoffroy et al. (2013b). In this model the Earth's climate system is made up of two layers that exchange heat with each other. The upper (surface) layer is forced by ΔF_e and the heat propagates into the deeper layer slowly. Time-dependent temperature development in each layer is described by a simple differential equation.

$$C_s \frac{\mathrm{d}\Delta T_s}{\mathrm{d}t} = \Delta F_e(t) - |\alpha_{FP}|\Delta T_s - \epsilon_o \gamma_o (\Delta T_s - \Delta T_d) \tag{3.18}$$

$$C_d \frac{\mathrm{d}\Delta T_d}{\mathrm{d}t} = \gamma_o (\Delta T_s - \Delta T_d) \tag{3.19}$$

The two delta-temperature variables ΔT_s and ΔT_d are the respective temperature anomalies from the climatic equilibria at the surface and deeper ocean layer. C_s and C_d are the specific heat capacities of the two layers in $\mathrm{W\,yr\,m^{-2}\,K^{-1}}$. $\Delta F_e(t)$ is the time-dependent radiative forcing and α_{FP} is the global feedback parameter. The two parameters ϵ_o for deeper ocean heat uptake efficacy and γ_o as an ocean heat transfer coefficient further describe the inertia of the system.

These constant parameters can be derived from general circulation models to calibrate the simple climate model. Smith et al. 2021a used models of the CMIP6 (Eyring et al. 2016) to arrive at the values for these parameters as summarised in Table 3.2 below.

Table 3.2: Two layer emulator parameters after (Smith et al. 2021a)

Parameter	Value	Unit
C_s	8.1 ± 1.0	$\mathrm{W\ yr\ m^{-2}\ K^{-1}}$
C_d	110 ± 63	$\mathrm{W\ yr\ m^{-2}\ K^{-1}}$
α_{FP}	1.33 ± 0.5	$\mathrm{W\ m^{-2}\ K^{-1}}$
ϵ_o	1.34 ± 0.41	dimensionless
γ_o	0.62 ± 0.13	$\mathrm{W\ m^{-2}\ K^{-1}}$

This is a system of two coupled differential equations describing the temporal evolution of two layer-mean temperatures. From comparing the model to observations, the upper-layer temperature T_s is set equal to global mean surface air temperature (GSAT) and the deeper layer temperature T_d is taken as a proxy on deeper ocean heat content. The two terms on the left sides of Equation (3.18) and 3.19 can be translated to the observed heat content increase rates in the upper and deeper ocean. The sum of the two integrals of these terms represents an approximate model result for comparison with observed EEU.

It is to be noted that the specific interpretation which layers of the actual climate system are represented by this simple model is an empirical choice to reasonably match observed surface and ocean temperature structures.

4 Data acquisition and analysis

4.1 Annual data and uncertainties

Earth energy uptake

EEU is the key variable used in this study to assess decadal EEI derived from the individual heat content increase rates in the four spheres of the climate system. The heat content data used in this work have been combined from various sources. Ocean heat content is derived from observational data by the Institute of Atmospheric Physics (IAP) at the Chinese Academy of Sciences (Cheng et al. 2021) and reanalysis data from Ocean Reanalysis System 5 (ORAS5) by Zuo et al. (2019). The presented uncertainties for ocean heat content arise from different sources in the two datasets used. Since ORAS5 is a reanalysis data set, it has been run with five different parameter sets to account for variability in the ocean model used. Uncertainty can therefore be assessed through the standard deviation of the spread between the five runs of the ocean model as outlined in Zuo et al. (2019).

IAP data relies mostly on expandable bathythermatograph (XBT) measurements and uncertainties account for errors in the measurement as well as interpolation errors in undersampled regions. Error calculation and bias correction of the observational data by IAP is described in Cheng and Zhu 2016. The mean error from the last decade has been used on data up to 2020. This makes the uncertainties presented in this study very different from OHC uncertainty in other studies like Schuckmann et al. 2020. The authors there presented uncertainties derived from the differences between datasets from a number of individual research groups.

Land heat content and cryosphere energy uptake are taken from Schuckmann et al. 2020 together with their presented uncertainties. These are given as uncertainties of the energy increase, i.e. the rate of change, resulting in the cumulative character of the presented LHC and CEU uncertainties.

Atmospheric heat content was provided by the Wegener Center for Climate and Global Change (Kirchengast et al. 2019; Gorfer 2022) to provide the most recent data up to 2020. Uncertainties were taken from Schuckmann et al. 2020 and extended to 2020. This data uses the reanalyses ERA-5 (Hersbach et al. 2020), MERRA-2 (Gelaro et al. 2017) and JMA-55 (Kobayashi et al. 2015) as well as the Wegener Center radio occultation and radio sonde record to provide the most accurate picture of atmospheric heat content. Additionally, the effect of El Niño–Southern Oscillation (ENSO) was regressed out, since this work only focuses on decadal timescales and ENSO would add inter-annual variability in the AHC timeseries.

The energy uptake in all four spheres of the climate system was used to calculate total EEU. In Figure 4.1 absolute heat contents are shown in ZJ versus the 1958-1962 baseline. Since AHC, CEU and LHC are very small in comparison to the ocean heat contents, they are shown seperately in a smaller panel. The uppermost (UM) ocean holds the largest part of energy accumulation before 1992, when the ocean heat content below the UM layer (OHCbelowUMOHC) eventually becomes larger.

All terms together consitute the Earth Energy Upatake (EEU) given relative to the 1958-1962 baseline. The UM layer comprises the water column of the uppermost 300 m. The OHCbelowUMOHC contains all layers below, i.e. deep ocean heat content for depths greater than 2000 m (DOHC), intermediate ocean heat content (IOHC) between 700 m and 2000 m and the lower 400 m of the upper ocean (UOHC). All of these data are from IAP and ORAS5. ORAS5 data has been used for depts up to 700 m, while IAP data is used for OHC up to 2000 m. DOHC is modeled linearly from 1990 on with a slope of 1.15 ± 0.57 ZJ yr^{-1} as presented in Schuckmann et al. 2020. For a more realistic and differentiable picture of the DOHC an 11-year running mean was applied to smooth out the sharp increase from a constant zero DOHC before and then a linearly increasing one in the years after.

In Figure 4.1 it can be seen that since the 1970s the energy budget anomaly has been positive. Ocean observations have vastly improved at the same time, reducing the errors in the data and more clearly approving the positive signal arising from the positive imbalance. In absolute terms the OHCbelowUMOHC surpassed the heat contained in the UM layer in 1992. This effect holds to this day and OHCbelowUMOHC is rising even faster than UMOHC. The rate of change can better be seen in the decadal mean trends in Section 4.2. For extending the data to 2020, AHC was recalculcalated with updated reanalysis and radio occultation data, IAP ocean data was used up to 2020 as well and the land and cryosphere components were extrapolated linearly.

Atmospheric heat content has reached an energy surplus relative to 1960 of 6 ± 2 ZJ, LHC following our methods has reached 25 ± 6 ZJ and the energy utilized to melt ice is 16 ± 2 ZJ. The ocean holds the greatest part of heat and the uppermost ocean already has taken up 159 ± 3ZJ of heat in the last 61 years. However, since in the ocean heat is constantly being mixed to the deeper layers, OHCbelowUMOHC holds 223 ± 13 ZJ as per 2020. This data show that in the period from 1960 to 2020 the total energy accumulated (EEU)has been 429 ± 14 ZJ.

Radiative forcing

For the balance equation (3.3) also radiative forcing is required on a global mean and annual resolution. The data in Figure 4.2 have been collected from a number of sources and put together in categories. ERF-NAT is made up of volcanic (Luo 2018; Kovilakam et al. 2020) and solar (Coddington et al. 2015; Yeo et al. 2017) radiative forcing . The errors for solar forcing arise mostly from the observation

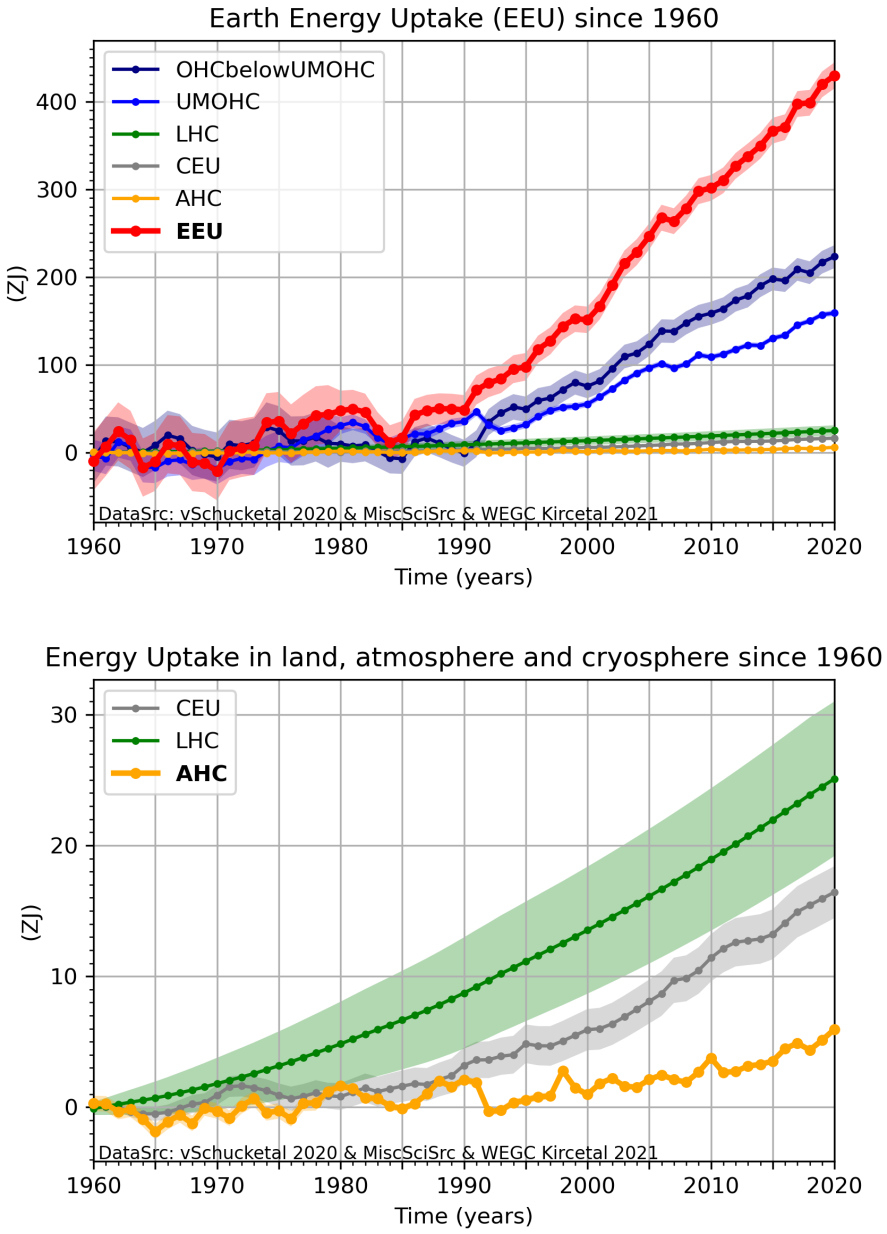


Figure 4.1: Earth energy uptake (EEU) since 1960. *Top*: Energy uptake is shown in ZJ in five domains of the climate system together with 90% CI corridors. Ocean heat content below uppermost ocean (OHCbelowUMOHC), ocean heat content in the uppermost (top 300 m) of the ocean (UMOHC), land heat content (LHC), cryosphere energy uptake (CEU) and atmospheric heat content (AHC). *Bottom*: Energy Uptake in land, atmosphere and cryosphere since 1960. This is a zoom into the top panel to highlight the changes of these small quantities together with their 90% CI corridors.

methods and the factors used to convert TSI to ERF. In the volcanic forcing time series errors account in the largest part for the standard deviation of the scaling factor.

ERF-OANT accounts for other anthropogenic forcings arising from stratospheric water vapour (Gulev et al. 2021), which is proportional to CH_4 forcing, contrails (Lee et al. 2021), black carbon on snow (Hoesly et al. 2018), land use (Ghimire et al. 2014) and ozone forcing (Skeie et al. 2020).

Aerosol forcings from aerosol-radiation and aerosol-cloud interactions are shown together as total ERF-AER from Smith et al. 2021b together with the uncertainties provided by the authors. This aerosol forcing dataset is a model-backed result, that has been studied with different initial conditions and was constrained using a two-layer energy balance model (see Section 3.5) and the energy budget by Schuckmann et al. 2020. Therefore uncertainties derive from the parameters used in the radiative transfer and in the energy balance model.

Radiative forcing from further non CO_2 greenhouse gases (FGHG) take into account CH_4, N_2O, CFC-11, CFC-12 and from 1979 onwards also 15 minor greenhouse gas forcings (HCFC-22, CFC-113, HCFC-141b, CCl4, HCFC-142b, CH3CCl3, H-1211, H-1301, H-2402, HFC-134a, HFC-152a, HFC-143a, HFC-125, HFC-23 and SF6) from Butler and Montzka (2021). The mole fractions for all gases before 1979 were exclusively taken from Meinshausen et al. (2017) and after that combined with data from Butler and Montzka (2021). The same applies to the forcing from CO_2. The computation of ERF using the greenhouse gas mole fractions follows the formulae presented in Section 3.2.

ERF-NAT accounts for the small solar forcing component that lies in the order of 0.1 $\mathrm{W\,m^{-2}}$ and the episodic volcanic cooling component that reached -1.8 ± 0.5 $\mathrm{W\,m^{-2}}$ in 1992 following the eruption of Mt Pinatubo. The sum of the two was -1.7 ± 0.5 $\mathrm{W\,m^{-2}}$ in the same year. The mean of ERF-NAT, however, is zero over the whole period from 1960 to 2020. ERF-OANT is dominated by the ozone component and has risen from 0.1 ± 0.1 $\mathrm{W\,m^{-2}}$ in 1960 to 0.5 ± 0.3 $\mathrm{W\,m^{-2}}$ in 2020. The cooling effect of ERF-AER was strongest in 1991 at -1.5 ± 0.9 $\mathrm{W\,m^{-2}}$ but has become less negative in the last decades. In 2020 it is standing at -1.1 ± 0.6 $\mathrm{W\,m^{-2}}$ and it is expected to become less negative in the future following all scenarios shown in Lund et al. (2019).

GHG forcings are the strongest driver of climate change and present the greatest forcing terms. ERF-CO2 alone has surpassed 2 $\mathrm{W\,m^{-2}}$ and reached 2.1 ± 0.3 $\mathrm{W\,m^{-2}}$ in 2020. In 1960 it was still 0.7 ± 0.1 $\mathrm{W\,m^{-2}}$. All other GHGs together (CH_4, N_2O and all synthetic GHGs) make up for 1.20 ± 0.07 $\mathrm{W\,m^{-2}}$ of the total forcing in 2020. The total ERF is 2.9 ± 0.8 $\mathrm{W\,m^{-2}}$ in the year 2020. From these numbers it can be concluded that CO_2 is responsible for more than 60 % of the total forcing excluding aerosol and natural forcings over the entire timespan.

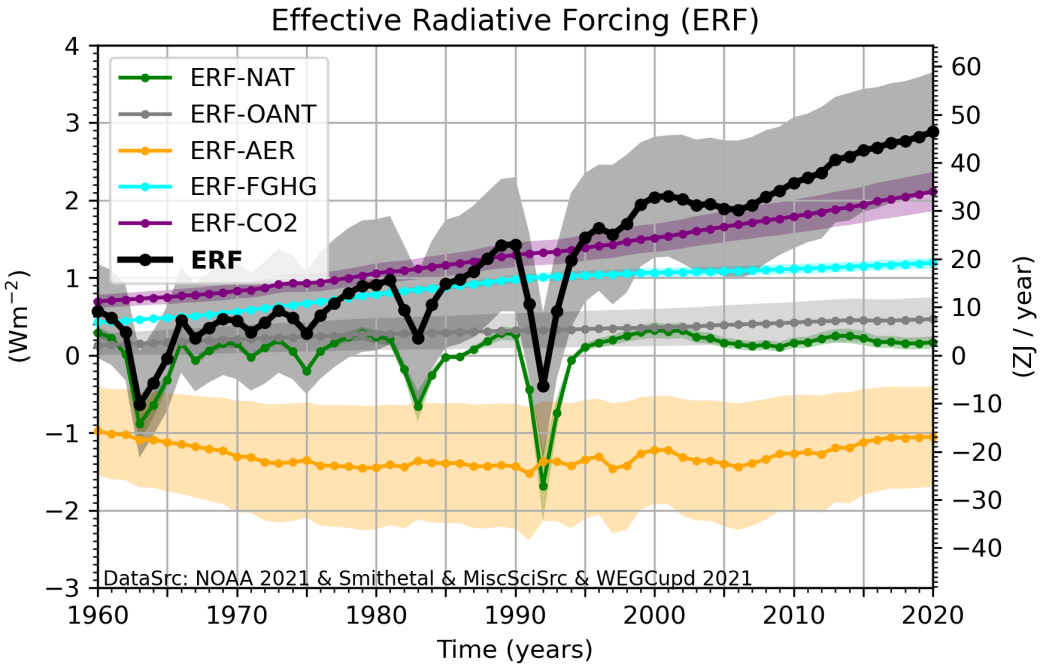


Figure 4.2: Effecticve radiative forcing (ERF). Shown are natural (ERF-NAT), other anthropogenic (ERF-OANT), aerosol (ERF-AER), further GHG (ERF-FGHG), CO_2 (ERF-CO2) and total ERF, together with 90% CI corridors.

Global surface air temperature

The most accurate data that flows into the balance equation comes from the global surface air temperature datasets. Figure 4.3 compares the three datasets examined in this study, although in the following chapters only the data by Morice et al. (2021) (HadCRUT5) will be used. GISTEMP Team (2021) and Hersbach et al. (2020) also provide global surface air temperature that agrees very well with the HadCRUT5 data. However, Morice et al. 2021 provide an ensemble of 200 realizations of the data, which makes it more suitable for studying uncertainties in the data. It is seen in Figure 4.3 that all three datasets do not deviate from their common mean by more than 0.05 °C, neither does the 200-member ensemble by Morice et al. 2021. This shows that GSAT is the most accurately known metric of global warming to this day. Moreover, it has the greatest importance for human life, since we live on the surface, which is why a close and accurate study has been established since the beginning of meteorological record keeping. (Gulev et al. 2021)

4.2 Decadal anthropogenic imprints

Using heat content data from Figure 4.1 the EEI has been calculated as a decadal mean in the time from 1965 to 2015. This was done by calculating the slope

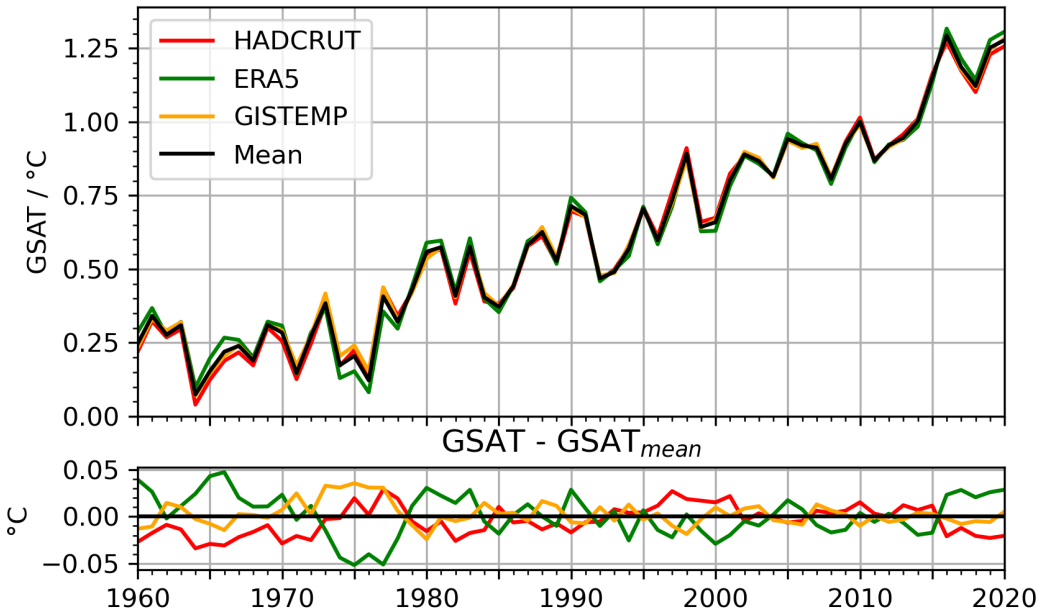


Figure 4.3: Global Surface Air Temperature (GSAT) from HadCRUT5 (Morice et al. 2021), ERA-5 (Hersbach et al. 2020) and GISTEMP (Lenssen et al. 2019). The small panel shows the differences of each dataset to the mean curve of all.

of a 11-year interval around every year. The adjacent five years of each year together with the year itself are weighted equally and an ordinary least squares fit is performed. The slope of this fit represents the decadal rate of change in each point. The slope standard error is taken as the error of each slope in an ensemble of gaussian distributed points around every point on a curve. The standard deviation used for the Gaussian is the standard error of the EEU data.

Figure 4.4 shows the increase rates of heat content in the five defined domains. AHCI is the atmospheric heat content increase rate, which has been shown by Kirchengast et al. (2019) to correlate well with the uppermost and topmost (upper 100 m) of the ocean. It also presents the strongest interannual variability due to the small specfic heat capacity of the atmosphere. Land heat content and cryosphere energy uptake increase rates (LHCI, CEUI) are less variable on this timescale. The ocean heat content increase rates generally have timescales of around pentades. These two increase rates are strongly influenced by the large oceanic inertia. On the decadal timescale in Figure 4.4, the OHCIbelowUMOHCI became larger than UMOHCI by the mid-1980s and it stays so to this day. This means that the deeper oceans meanwhile are accumulating a larger amount of heat than the uppermost ocean in the same time interval since 1960.

The heat wave has reached even the deepest oceans, which is why the linear trend estimate for DOHC was applied in Schuckmann et al. (2020). Nevertheless, it has been very difficult to assess this heat uptake rate since not enough measurements are available in these large depths below 2000 m. In the last years the Argo

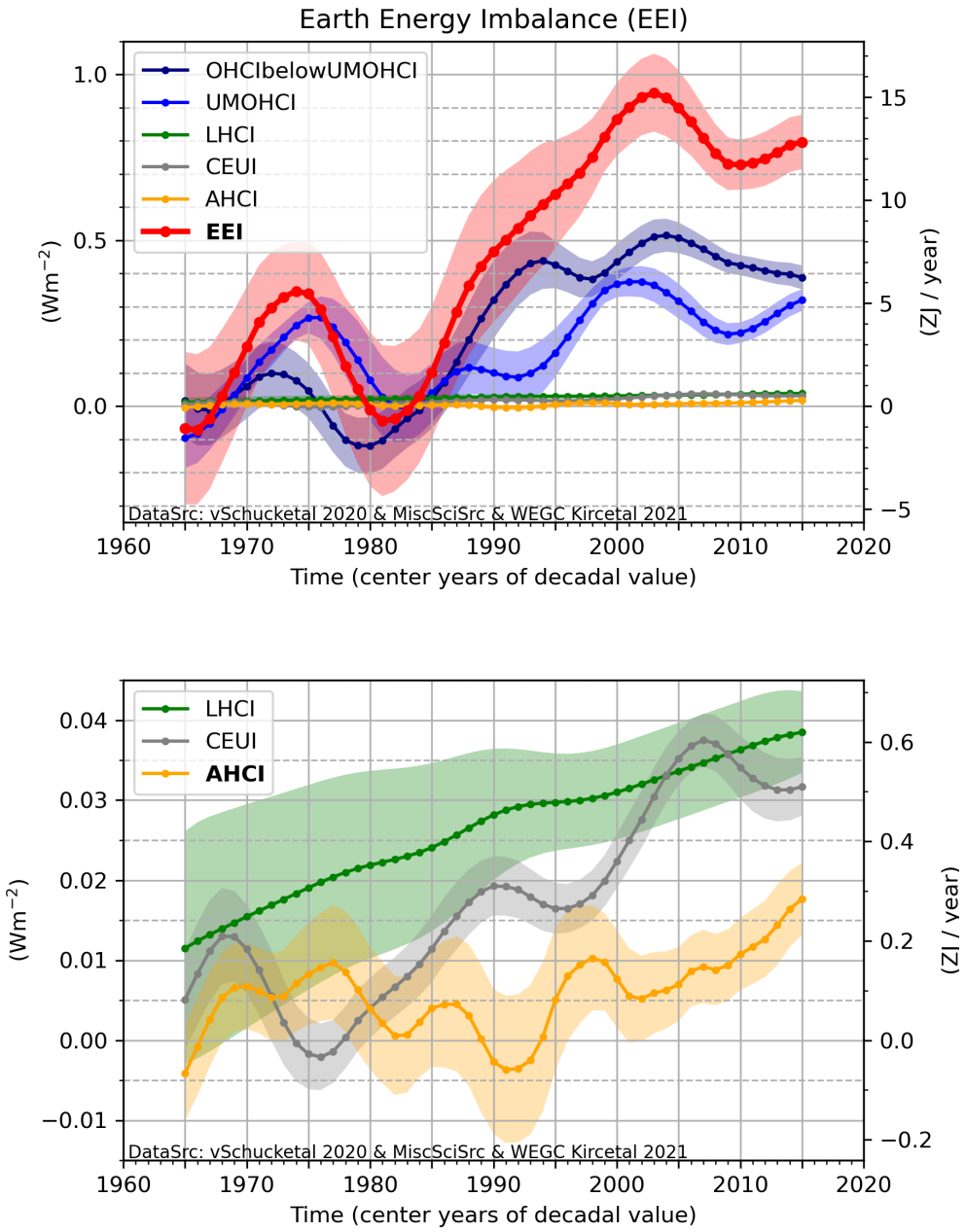


Figure 4.4: *Top*: Decadal-mean Earth Energy Imbalance (EEI) and heat content/ energy uptake increase rates in all subsystems of the climate system together with 90% CI corridors. *Bottom*: Decadal-mean increase rates of atmospheric (AHCI), land (LHC) heat contents and cryosphere energy uptake (CEUI). This is a zoom into the top panel better showing the small increase rates in these subsystems together with their 90% CI corridors.

network is expanding to the deep oceans to improve our knowledge about DOHC and eventually its contribution to EEI (Roemmich et al. 2019).

The sum of all components, represented as EEI, had reached close to 1 $\mathrm{W\,m^{-2}}$ in the early 2000s. Between 1980 and the beginning of the 2000s it was steadily rising. This signals that climate warming has been accelerating over this period. The period before 1980 bears large uncertainties and can therefore not be discussed in detail. It is certain that the climate has left its state of balance since at least the 1970s. After about 2010 EEI has started to rise again and it will probably continue in the future as will be seen in Chapter 6. In Figure 4.4 (bottom panel) AHCI is shown separately together with LHCI and CEUI to highlight its large variability. Relative to its trend it has the largest interannual (not shown) and annual variability. However, the signal shown here, wich has been corrected for effects of the El-Niño- Southern Oscillation (ENSO) proves that it has been rising steadily since 2000. Especially in the years after 2010 the decadal signal shows a very fast increase. This is due to the slower heat increase in the ocean leading to the trapping of more heat in the atmosphere. The LHCI shows an almost linear increase and CEUI shows large inertia, too.

4.3 Decadal radiative forcing and response

For comparison with the EEI from above, ERF and RRE were calculated on a decadal-mean basis as well. In Figure 4.5 the ERF excluding volcanic components is decadally (11-year running mean) smoothed and RREd is calculated as a product of 1.4 $\mathrm{W\,m^{-2}\,K^{-1}}$ with the decadal-mean GSAT timeseries of Morice et al. (2021) using the same decadal filtering as for ERF. The constant 1.4 $\mathrm{W\,m^{-2}}$, further discussed in Chapter 5 below, is taken as a best estimate for the climate feedback parameter α_{FP} assuming no uncertainty.

In this manner the shown 90% CI corridors in Figure 4.5 incorporate only input-data-related uncertainties and not the ones from physical process understanding that might arise in the climate feedback parameter. The difference of ERFd and RREd on the decadal timescale (ERFdminusRREd) shows far less variability than the in-situ derived EEId but this stays within the uncertainty of ERFdminusRREd. After center year 2010 the two variables agree very well, likely also due to the large improvements in ocean observation since the advent of Argo's global coverage in 2005.

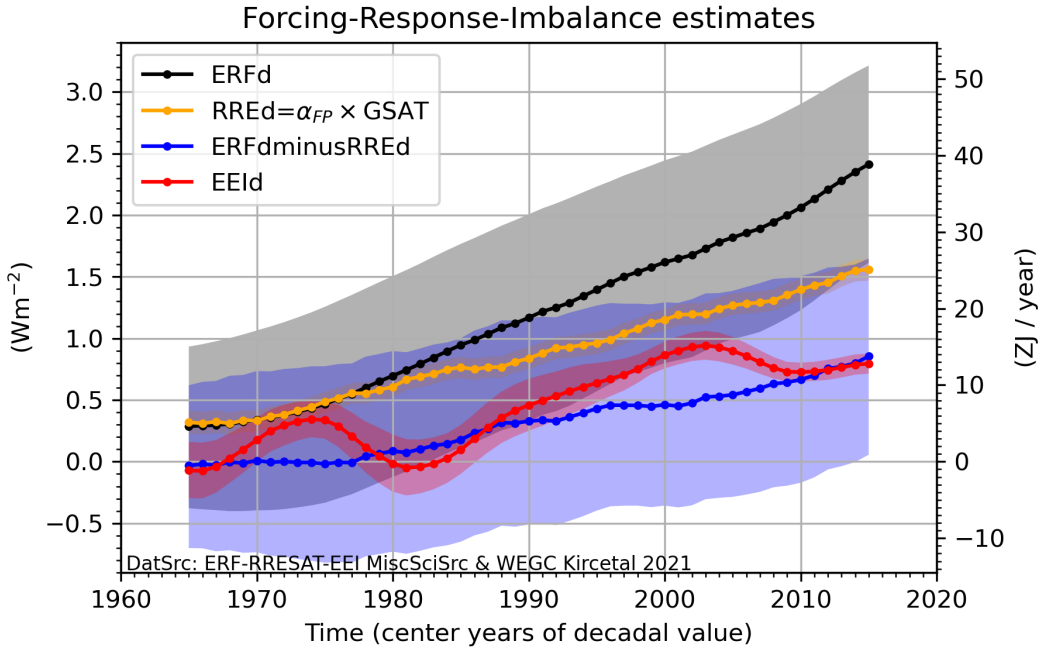


Figure 4.5: Forcing-Response-Imbalance estimates. All curves are decadal-mean averages, uncertainty corridors represent 90% CIs. The black line represents decadal-mean ERF, the yellow line decadal-mean GSAT multiplied with a constant of 1.4 $\mathrm{W\,m^{-2}\,K^{-1}}$ as a best estimate of the climate feedback parameter. Blue shows the difference of these two curves as a comparison with the independent EEI in red.

4.4 Comparison of observational data sets

OHC datasets

This section will show the differences among the ocean observation datasets used, since these bear the largest uncertainties. The data used come from ORAS5 (Zuo et al. 2019) and IAP data (Cheng et al. 2021) and have been prepared for the purpose by Kirchengast et al. (2019) and Gorfer (2022). It is important too keep in mind, that ORAS5 is composed of an ensemble with 5 realizations, where only the mean curve is shown. Figure 4.6 shows these data together with the IAP data from 1980 onwards. ORAS5 is used in this study from 1980 to 2019, which is the last available year. IAP data is available from 1940 to 2020, but not fully shown here to make the differences with ORAS5 clearer. Data agree very well for TMOHC (top 100 m of ocean), with differences of about 10 ZJ in the early record. Between 1983 and 2015 the two curves do not show major discrepancies, whereas in the three most recent years are the only ones where an offset is present again.

UMOHC agrees less with a difference of almost 20 ZJ in the year 1981 and a following underestimation of UMOHC in comparison to the IAP record until 2000. This is followed by a period where ORAS5 has larger values again and again from 2015 on they keep increasing faster in contrast to ORAS5. Additionally,

the ORAS5 data presents less variability on annual scales. IAP data rises nearly linearly since 1995, which is not true for ORAS5.

In the bottom panel the deepest available layer for ORAS5 is shown, which is the lower part of the upper ocean covering depths of 300 m to 700 m. Probably owing to a poorer representation in the ocean model used for the reanalysis, OHC in this depth layer shows only long-term variability in ORAS5. IAP data also relies on observations here, which makes the signal more variable. In the years 1980-1985 OHC by ORAS5 is larger. From 1986 to 2003 it is smaller and does not show the variability that IAP represents. From 2004 onwards OHC by ORAS5 is almost constantly rising faster than what is seen from IAP data.

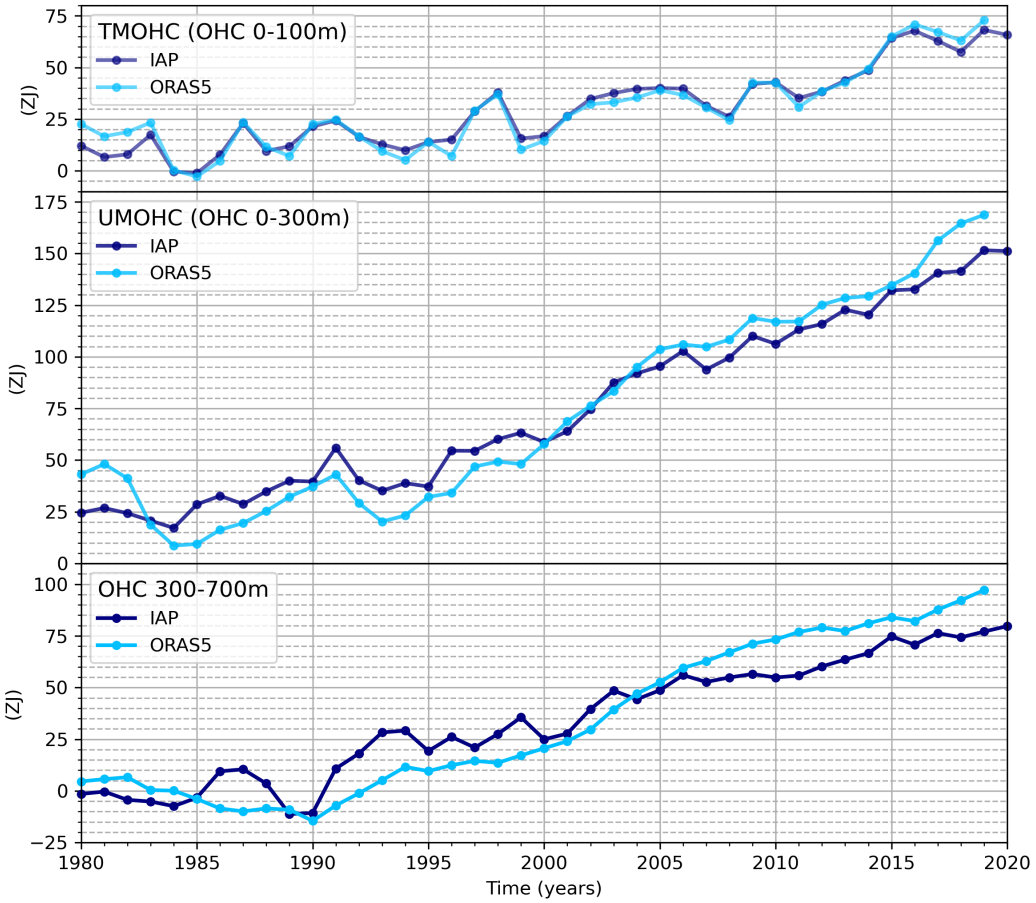


Figure 4.6: Comparison of TMOHC (0-100 m), UMOHC (0-300 m) and the bottom upper-ocean OHC at 300-700 m from IAP data and ORAS5 data.

GSAT and OHCI

In the previous section the quality of individual datasets has been assessed. However, it is important to study, whether data from temperature and heat content measurements agree, too. To do that Figure 4.7 shows the temperature rate of change in relation to the heat content increase rate in the first 100 m of the water column, the topmost (TM) ocean and the UM layer together with atmosphere contributions. Temperature rate of change is multiplied by a constant specific heat capacity of the oceanic mixing layer as used in the two-layer energy budget model. C_{mix} is equal to 8.1±1.6 $\mathrm{W\,yr\,m^{-2}\,K^{-1}}$ following Smith et al. (2021a). Corridors represent the 95 % confidence intervals of this constant. Temperature errors are not taken into account since GSAT has an error of only 0.05 K throughout the record. The plot shows a very good agreeement of the two timeseries of temperature and OHC change. It is only after 1990 that the 200 m below the TM oceans start to add a larger portion of heat that makes the UMOHCI series deviate strongly from TMOHCI and thus also from the surface air temprature trend.

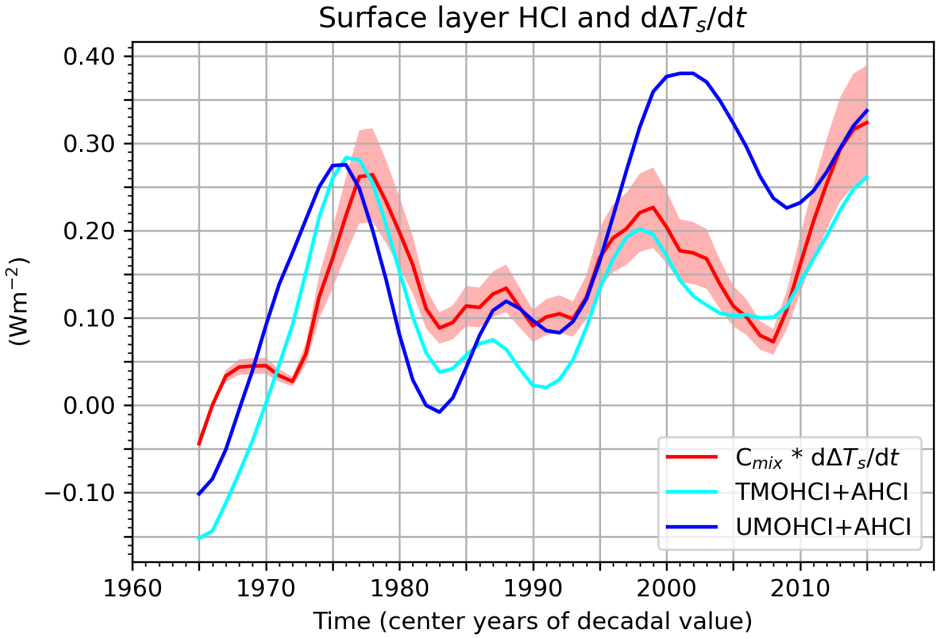


Figure 4.7: Sum of decadal-mean topmost (TM) and uppermost (UM) ocean with atmospheric (AHC) heat content increase compared to GSAT (T_s) increase with time with 90% CI corridor for the mixing laxer heat capacity C_{mix}.

5 Climate feedback parameter estimation

In the previous chapters the term climate feedback feedback parameter has already been mentioned several times. However, this chapter will outline the methods for assessing climate feedback across the literature and finally in this study. In the following the theoretical arguments will be discussed in further detail.

As stated in Equation (3.4) α_{FP} is the sum of all feedback terms. This means it takes into account all changes in climate variables that affect the radiation budget. These include apart from temperature change, also water vapour rise, changes in cloud processes, surface albedo, lapse rate and other changes such as ozone processes affected from the rising concentrations. Sherwood et al. (2020) represents α_{FP} as the sum of these terms.

$$\alpha_{FP} = \sum_f \alpha_f = \alpha_{\text{Planck}} + \alpha_{\text{WV, LR}} + \alpha_{\text{surf. albedo}} + \alpha_{\text{cloud}} + \alpha_{\text{other}} \tag{5.1}$$

Feedbacks can be negative or positive. Positive means that they enhance the effect on global temperatures, therefore increasing temperature change, whereas negative feedbacks hold back climate change. The strongest feedback, which is the Planck feedback, is negative. It represents the increased emission of IR radiation by Earth's surface in response to a warming climate (Sherwood et al. 2020). Due to the increased radiation the surface counteracts in response to the external forcing, thus compensating against the forcing. α_{Planck}=-3.2 ± 0.2 W m^{-2} K^{-1} following Sherwood et al. (2020).

In a warming climate water vapour concentration rises following the Clausius-Clapeyron relationship. This means an exponential increase with temperature. Since water vapour in the upper troposphere absorbs both SW and LW radiation it produces a positive feedback by trapping more heat in the atmosphere through decreased LW emission at the TOA. From satellite observations this feedback has been assessed to lie at α_{WV}=1.77 ± 0.33 W m^{-2} K^{-1} (Liu et al. 2018). The lapse rate is the gradient of temperature with altitude. Under a forcing, lapse rate is affected differently depending on the observed latitude. Generally, lapse rate feedback describes the changes in LW emission due to a nonuniform vertical temperature gradient. Low latitudes experience more warming in the upper troposphere due to the lapse rate following a moist adiabat. Rising surface temperatures in the tropics lead to even higher temperature anomalies in the upper troposphere. More LW radiation is emitted and therefore the feedback is negative. At high latitudes the surface warms stronger than the atmosphere and therefore lapse rate feedback in these regions is positive. Assessing lapse rate and water vapour

feedback independently is not useful, though, since the two are anti-correlated. Radiation to space depends strongly on relative humidity, but this changes only little under climate warming. Uncertainty in sum of the two feedbacks is thus lower than for the two individual feedbacks. Sherwood et al. (2020) gives a value of $\alpha_{\mathrm{WV,\ LR}}$=1.15±0.25 $\mathrm{W\,m^{-2}\,K^{-1}}$.

The overall lapse rate feedback is negative since the tropical effects dominate in the global mean. Global mean surface albedo affects the climate as well. Brighter surfaces reflect more SW radiation, so they tend to cool the surface. Warming, however, helps to decrease the area of frozen or snow-covered surfaces introducing a positive feedback. More warming means less bright surfaces, which in return leads to more SW absorption of the surface and an increase in GSAT. The magnitude of this feedback is about $\alpha_{\mathrm{surf.\ albedo}}$=0.30±0.25 $\mathrm{W\,m^{-2}\,K^{-1}}$ (Sherwood et al. 2020).

The feedback, that has been and remains most difficult to assess is cloud-related feedback. There are a number of processes that play a role in cloud feedbacks. Most of them affect the amount of cloud cover and its effect on the albedo. Less relative humidity usually means less clouds and finally leads to a decrease of the albedo. This is the case for most low clouds, which are observed to form less in a warmer climate, which in turn increases the warming. High clouds have a positive forcing, which is confirmed by observations and climate models. Their cloud tops can rise higher and become cooler, which leads to a decrease in emitted radiation. The only cloud-related feedback that might be negative is the one resulting from tropical anvil clouds. However, Sherwood et al. (2020) still give a mean estimate of zero. Going into detail on cloud feedbacks is beyond the scope of this work. Sherwood et al. (2020) assesses a total cloud feedback of α_{cloud}=0.45±0.55 $\mathrm{W\,m^{-2}\,K^{-1}}$.

From various lines of evidence such as process-understanding, theoretical arguments, global climate models and climate records Sherwood et al. (2020) arrive at the total mean estimate of α_{FP}=-1.30 ± 0.72 $\mathrm{W\,m^2\,K^{-1}}$, which has also been mentioned previously. Here we use the 90 % confidence range in contrast to the standard deviation in Section 3.3.

A comparison of an energy balance observational estimate with this value based on theory, observations and process-understanding is not trivial, but valid, as will be outlined in the following. In this study an energy budget approach is taken to compute climate feedback. This has also been done in a series of previous studies (Forster 2016; Gregory et al. 2002; Otto et al. 2013). In contrast to the previously mentioned study of individual feedbacks, in the following the equations from Section 3.1 are rearranged to give an expression for α_{FP},

$$\alpha_{FP} = \frac{\Delta F_e - \Delta N}{\Delta T_s}. \tag{5.2}$$

This equation can only be valid on decadal timescales, since ΔN is decadal-mean by formulation due to the methods described earlier concerning its calculation. This means that also ΔF_e and ΔT_s are decadal-mean averages, which is achieved by inserting the values used in Section 4.3, namely the decadal GSAT from RREd and the decadal-mean ERFd. As stated, EEI does not need to be considered against a

reference period, since it is the fundamental quantity that is only present if climate change is transient. The decadal temperature change ΔT_s and the effective forcing ΔF_e are anomalies against the preindustrial period.

5.1 Climate sensitivity framework

The climate sensitivity is not an estimate of transient climate response (TCR), which is a widely used climate metric not accounting for the energy imbalance. It is the product of forced temperature change and the effective radiative forcing that would arise from a doubling of CO_2, divided by the total radiative forcing.

$$\mathrm{TCR} = \frac{\Delta F_{2\times \mathrm{CO}_2} \Delta T_s}{\Delta F_e} \tag{5.3}$$

This does not account for the imbalance term and therefore represents only the transient response of the climate but not the effect on energy balance. It assumes a constant $\Delta N/\Delta T_s$ ratio, which is the same as in the 70th year of a climate simulation with an increase of CO_2 concentrations at 1% per year (Otto et al. 2013).

Similarly the Earth Climate Sensitivity (ECS) is defined, but now accounting for energy imbalance, and providing an estimate of climate sensitivity at equilibrium conditions.

$$\mathrm{ECS} = \frac{\Delta F_{2\times \mathrm{CO}_2} \Delta T_s}{\Delta F - \Delta N} \tag{5.4}$$

Comparison with Equation (5.2) shows that α_{FP} and ECS are inversely proportional, with a conversion factor $\Delta F_{2\times \mathrm{CO}_2}$.

$$\alpha_{FP} = \frac{\Delta F_{2\times \mathrm{CO}_2}}{\mathrm{ECS}} \tag{5.5}$$

The forcing resulting from CO_2 doubling $\Delta F_{2\times \mathrm{CO}_2}$ can be calculated using the equations from Section 3.2, yielding 3.93 ± 0.47 W m^{-2} (Forster et al. 2021).

5.2 Observational constraints

Using data that is mostly based on observations a constraint on the climate feedback parameter can be drawn by taking an average over well-observed periods of global warming, where a linear approximation on the warming is valid. This is the case for the last 45 years of observations. Global temperature observations have a near constant uncertainty of about 0.05 K, EEI errors have been decreased substantially and parallel to that the coverage of ocean observations reached almost the whole ocean. Undersampled regions can be interpolated using statistical methods (Cheng et al. 2021). Furthermore, ERF can be calculated with updated formulae and very accurate emission observations are available for the GHGs. The use of the

up-to-date model-based and observation-constrained aerosol forcing by Smith et al. (2021b) allows a reasonably accurate calculation of ERF as seen in the previous chapter. Combining these results a time series of α_{FP} can be estimated.

5.3 Time dependent evolution

Figure 5.1 shows the results of combining these three datasets to derive the climate feedback parameter. The early 1980s were still dominated by large uncertainties, but a significant improvement of data is observed along time. The mean value of Sherwood et al. (2020) is shown together with its 90% confidence interval as a corridor and the related values in the figure legend. Time-dependent α_{FP} from this study is shown as "α_{FP} using GCCI-CWM data".

This study has provided the data for the Graz Climate Change Indicator (GCCI) data portal, making it publicly available (Kirchengast et al. 2021). Uncertainties of the data used for this study's estimate are depicted in corridors of different colors. The lighter corridor represents the full 90% confidence interval as it results from the combined uncertainties. A darker corridor has been chosen to show the part of the uncertainty corridor that lies inside the assessed interval by Forster et al. (2021). The innermost corridor represents the variation of the decadal mean inferred by temporal variability over the 1980-2015.

Observational data seem to give a higher estimate for α_{FP} than process-understanding. It has been argued that due to the observed pattern of sea surface warming, the historical record might not be suitable to derive an estimate of equilibrium climate feedback. However, the estimates of this "pattern effect" (Dong et al. 2020; Jiménez-de-la-Cuesta and Mauritsen 2019; Sherwood et al. 2020) remain highly uncertain, which is why it has not been considered in this work.

A comparison with the α_{FP} estimates in Forster (2016) shows that the timeframe used for the calculation of the feedback parameter leads to large differences in the absolute value of the result. One of the earlier studies (Gregory et al. 2002) gives a value of 0.6 $\mathrm{W\,m^{-2}\,K^{-1}}$ for the period 1957-1994, whereas Otto et al. (2013) arrives at 1.72 $\mathrm{W\,m^{-2}\,K^{-1}}$ using data from 1970-2009. Schwartz (2012) used almost the same period (1965-2009) and gives a range of 0.86 - 3.22 $\mathrm{W\,m^{-2}\,K^{-1}}$.

5.4 Role of Earth Energy Imbalance

The uncertainty of EEI plays a key role for computing α_{FP} from energy balance. Since its improvement has led to better estimates in the last decades it has become possible to narrow the range of possible feedback parameters. On the ERF side aerosol forcing still will need to be improved, but the ERF presents less variability in contrast to EEI. Energy imbalance requires knowledge of very accurate heat contents on a global level to yield realistic results. Otherwise the use for a climate feedback estimation is not justified. The true global coverage for past records can only be achieved thorugh interpolation methods. In some studies as Schuckmann

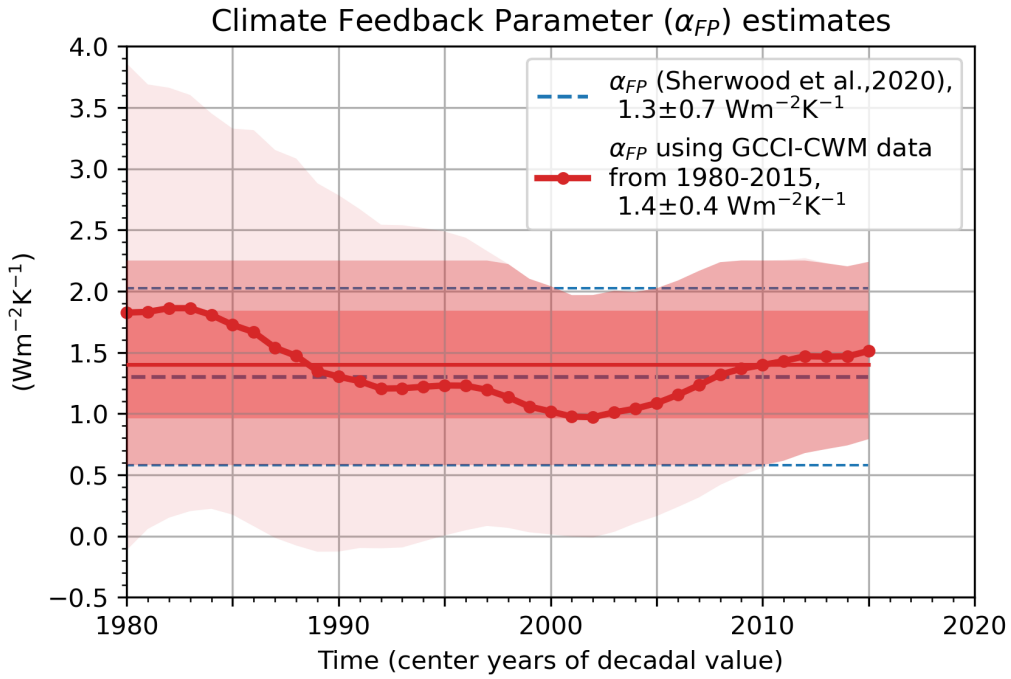


Figure 5.1: Climate feedback parameter α_{FP} estimates inferred from energy balance. An estimate of Sherwood et al. (2020) is shown in dashed-blue together with 90% CIs. In red the estimate from the methods used in this study are shown with light red corridors representing 90% confidence intervals, daker light-red showing plausible values according to Forster et al. (2021). The red line represents the mean with a dark red corridor accounting for 90% CIs of the inferred uncertainty based on the 1980-2015 variability estimation.

et al. (2020) the focus lies on a more exact measurement of heat contents omitting parts of the ocean that have been undersampled. This study, however, has the goal of calculating a full global estimate of EEI by using data from Cheng et al. (2021) that had been corrected with the methods used by IAP. This correction scheme is the most widely accepted one in the community to this day but still has large uncertainties in the pre-1980 period.

Since EEI has a large natural variability from volcanic and solar forcing the filtering method used plays a large role, too. By limiting the interest in a decadal estimate of EEI with the 11-year running mean filter that uses equal weights the major variability components disappear. This method allows a comparison with the smooth data from GSAT and ERF.

6 Global temperature and energy imbalance modeling

In the following chapter the results of the simple energy balance model presented in Section 3.5 will be presented. This model is also used in the 6th Assessment Report of the IPCC to simulate short-term temperature evolution. The model needs the input parameters C_s, C_d, α_{FP}, ϵ_o and γ_o. In line with the IPCC approach these were sampled from Gaussian distributions constructed with the mean and standard deviations from Table 3.1. Furthermore it requires knowledge of annual ERF, for which the ERF from Chapter 4 was used. In order to achieve results that can be compared to the observation-based approach above for determining α_{FP}, the forcing used here excludes the episodic volcanic forcing, however, that acts on the inter-annual rather than the decadal scale.

In this study, the 2-layer model has been used to model historical temperature change in the period from 1960 to 2020 as well as EEU, EEI and the deeper ocean temperature change ΔT_{deeper}. These results have been combined to yield an estimate of α_{FP}, based on the time period from 1980 to 2015.

6.1 Consistency with observational data

The first step was to check the model's performance in modeling historical climatic change. Therefore the ERF data used in Chapter 4 were extended back to 1750 with ERF from Smith et al. (2021a) along with their uncertainty estimates. The period of interest, however, is 1960 to 2020. The back-extension only helps calibrate the model. In Figure 6.1 it is visible that this model acts like a smoothing filter and shows little variability on inter-annual scales. The modeled GSAT seems fairly smooth at sub-decadal scales. However, looking at its time-derivative, EEI_{upper}, which can be interpreted as the Earth Energy Imbalance component resulting from the surface layer, there is still some inter-annual variability. Therefore this quantity was further decadally smoothed to make it more comparable to the EEI from observations. It appears to agree quite well with the sum of TMOHCI and AHCI from the mid-1990s to the mid-2000s, but since 2010 it agrees better with the sum of UMOHCI and AHCI.

This is expected, because the heat energy is continuously mixed to deeper ocean layers and therefore a larger water column has to be integrated to catch the imbalance term. The temperature of the deeper ocean layer, T_{deeper}, agrees very well in its mean with OHCbelowUMOHC divided by the deeper layer specific heat capacity C_d and the offset by the 1960 value of the modeled T_{deeper}. This is not

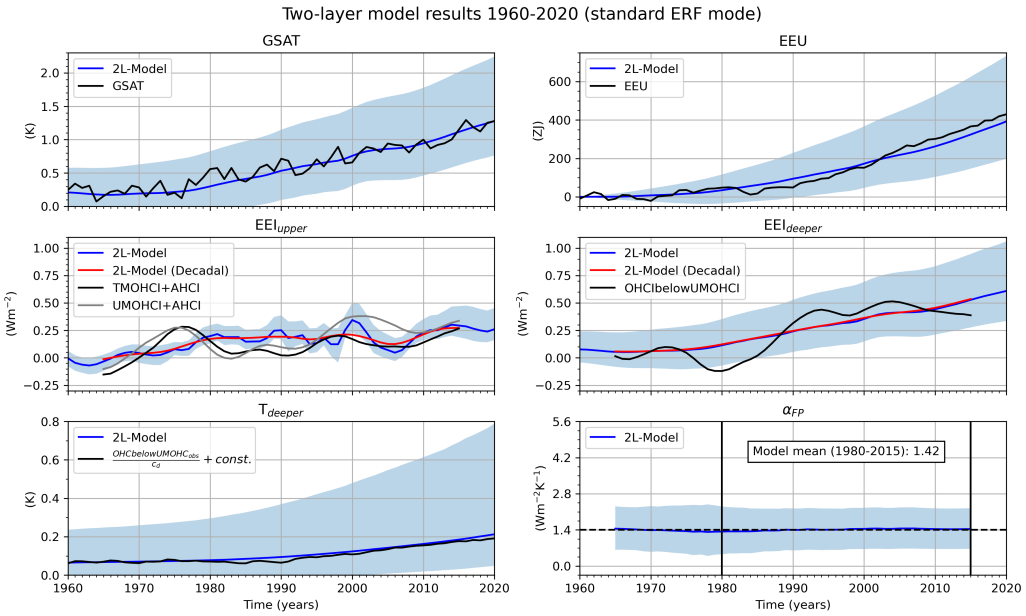


Figure 6.1: Two-layer model results 1960-2020 (standard ERF mode) with 90% CI corridors. Global Surface Air Temperature (GSAT) and Earth Energy Uptake (EEU) are shown in the top row. The contributions to EEI from the two layers EEI_{upper} and EEI_{deeper} are depicted in the middle row. The bottom row shows deeper-layer temperature (T_{deeper}) and the estimate for α_{FP} using model results and observations.

an independent value that is compared, but the time-dependent behavior of the two quantities shows very good correlation. Together with EEI_{deeper}, the integral of the total EEI gives EEU, which again shows a more smooth behavior in the model, but the comparison proves a good representation of EEU in the model. EEI_{deeper} is shown below EEU, together with its decadal-mean and the observed OHCIbelowUMOHCI. Due to the large inertia of the deeper ocean EEI_{deeper} is already very smooth and the decadal mean is not very different to the annual result. Taking together modeled EEI, GSAT, and the decadal-mean ERF, a very stable α_{FP} is derived with a 1980-2015 mean of 1.42. This result is very similar to the observation-based estimation in Chapter 5.

6.2 Probing the model under different drivers

Next, the model was modified to take other quantities as input parameters, while still sampling the remaining free parameters from the Gaussian distributions. First a surface-temperature-driven model mode was tested and then an energy imbalance-driven mode was implemented, too. This section shows the results of both of these modeling modes, where the version with temperature as input is termed "Preset GSAT mode" and the one taking Energy imbalance as input as

"Preset EEI mode". In the related figures the preset input quantity is always shown in green to distinguish it from the results.

Preset GSAT mode

In Figure 6.2 the results of driving the model using GSAT are shown. The temperature dataset by Morice et al. (2021) was used randomly, sampling 10000 realizations from their ensemble and using decadal means of temperature data from 1850 to 2020. Due to the small spread of these data especially on decadal timescales the uncertainty of the model results is also low. EEU shows very good agreement with observations before 1980 and after 2005 but in between the GSAT data tend to overestimate heat accumulation. EEI_{upper} and its decadal mean agree better with TMOHCI+AHCI than with the sum including UMOHCI. This is most probably related to the fact that TMOHCI has a stronger coupling to GSAT, given it comprises just the upper 100 m of ocean water.

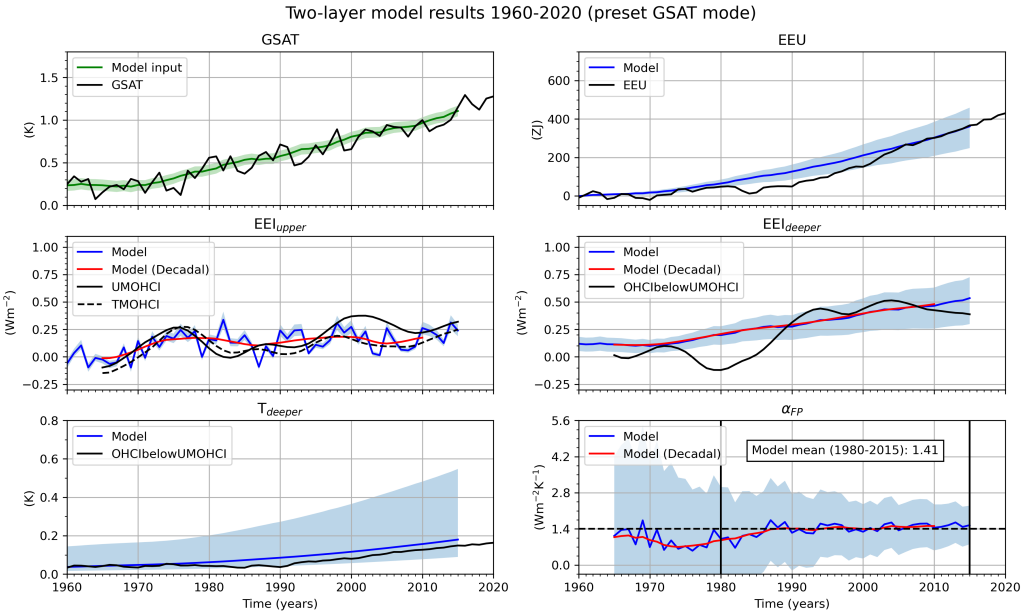


Figure 6.2: Two-layer model results 1960-2020 with prescribed GSAT (Preset GSAT mode) and 90% CI corridors. Global Surface Air Temperature (GSAT) and Earth Energy Uptake (EEU) are shown in the top row. The contributions to EEI from the two layers EEI_{upper} and EEI_{deeper} are depicted in the middle row. The bottom row shows deeper-layer temperature (T_{deeper}) and the estimate for α_{FP} using combined model results and observations.

EEI_{deeper} is again fairly smooth and agrees to the same extent with OHCIbelowUMOHCI as the one derived from the standard ERF mode of the model (Figure 6.1). T_{deep} compared to the OHCbelowUMOHC time series shows the missing energy that is also seen in EEU, as an offset to deeper ocean temperature

starting near 1980. Putting the data together, an estimate for α_{FP} that is just slightly lower than in the standard ERF mode (at $\alpha_{FP} = 1.41$) for the period 1980-2015 is derived. The comparison with the decadal value shows that since 1990 the climate feedback parameter derived by this method shows almost no transient variation, but only inter-annual noise from the GSAT dataset used.

Preset EEI mode

Inserting EEI data as input also gives results only of decadal-mean values, since it is already calculated as a decadal mean. An initial offset has to be introduced in order to achieve a temperature result that agrees with observations. This is done by sampling the offset temperature for the first timestep of the model from the distribution of temperatures in the first year used for the Preset GSAT mode and derived from Morice et al. (2021) data.

In Figure 6.3 the results for the Preset EEI mode are shown. Temperature results do not agree well between 1980 and 2005. This is due to the same effect that has been discussed previously. EEU data lacks a part of energy that is seen in the GSAT data set. Of course EEU and EEI agree quite perfectly in this mode, since this was used an input. Also the deeper ocean temperature agrees very well, since it is also directly connected to deeper ocean heat uptake.

Apart from GSAT only the feedback parameter allows for a comparison with an independent quantity. It is seen that using only EEI data gives unrealistic results before 1995. Since 2000, however, the uncertainty corridors based on ERF, GSAT and EEI begin to align showing a very significant decrease in uncertainty and a more plausible feedback parameter value. This is why the timespan for the mean has been reduced to include 1995-2015 in this section. This yields an α_{FP} of 1.37, which lies in the interval presented in Chapter 5. Further improvement of EEI observations could add greater value to this method of obtaining an estimate for the feedback parameter.

6.3 Climate change scenarios up to 2050

Using the two-layer energy balance model, also future climate scenarios can be inspected. This section presents the results of using ERF from the main Shared Socioeconomic Pathways (SSPs) up to 2050 to model the evolution of GSAT, EEU, EEI and T_{deep}. The model is used in its standard form with ERF excluding volcanic forcing as the driving variable. Results with the time-dependent volcanic component are shown only for historical data seperately. EEI is assessed as a decadal mean only in these results to highlight the long-term changes.

The upper left panel of Figure 6.4 shows the ERF timeseries used to calculate the model results. Until 2020 the observation-based ERF has been used to calculate model results from the historical record (hist) and from 2021 onwards the respective SSP scenario values are shown. These are denoted as e.g. SSP1-1.9, where SSP1 stands for the socioeconomic part of the scenario that is a sustainability path

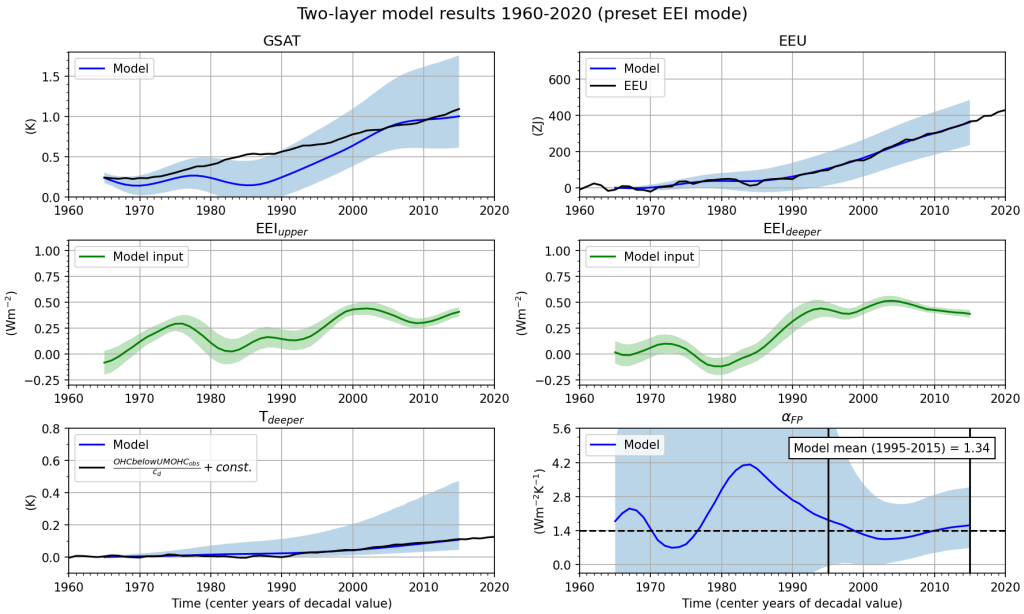


Figure 6.3: Two-layer model results 1960-2020 with prescribed EEI (Preset EEI mode) and 90% CI corridors. Global Surface Air Temperature (GSAT) and Earth Energy Uptake (EEU) are shown in the top row. The contributions to EEI from the two layers EEI_{upper} and EEI_{deeper} are depicted in the middle row. The bottom row shows deeper-layer temperature (T_{deeper}) and the estimate for α_{FP} using combined model results and observations.

in SSP1 and 1.9 stands for total ERF in 2100, which would be approximately 1.9 W m^{-2} in this case. SSP2 describes a middle-of-the-way scenario and SSP5 allows fossil-fuel development in the future (Meinshausen et al. 2020). These SSP scenarios have also been used in the IPCC assessment work by Forster et al. (2021).

Figure 6.4 top right panel shwos EEU. The scenario with the highest ERF, SSP5-8.5, reaches an EEU of about 1000 ZJ in the year 2050. This is more than a doubling compared to present-day values. All other scenarios lie below that. It is also observed that SSP5-8.5 tends to deviate faster from the other scenarios by continuing the trend of the last decades of observations.

For decadal-mean annual-mean EEI_{upper}, i.e. the surface-layer contribution to the EEI, the sustainability scenario SSP1-1.9 reaches zero already near 2045. This would mean that from 2050 onwards the deeper ocean might start to act as a heat source, warming the surface layer from below. SSP2-4.5 stops decreasing this variable at 2030 and remains almost constant at 0.2 W m^{-2} until the end of the period. The slightly lower SSP1-2.6 shows to decrease until 2045. Finally, the fossil-fuel development scenario continues to push EEI in the upper layer to 0.3 W m^{-2} in 2045.

Deeper-layer EEI has been shown to be more inert, but also increases much stronger under the worst-case scenario SSP5-8.5. It surpasses 1 W m^{-2} around 2040. The other scenarios follow almost the same development until 2030, but

deviate in the last years of the simulation, with taking EEI_{deeper} values between 0.7 and 0.9 W m^{-2} around 2045.

The modeled GSAT as the most crucial metric of climate change reaches between 1.6 and 2.5 K in 2050 under the preset ERF. Nevertheless, this shows how sustainable development gives hope to limit global warming. The worst-case already passes 2 K before the year 2040. Of course, the rise in deeper ocean temperature is not so big in absolute terms, but it could lead to significantly different futures for the global oceans between the scenarios.

It can be seen that only in the scenario SSP5-8.5 there are strong upwards trends in EEU, EEI, GSAT and T_{deeper}. The other scenarios tend to lower the rates of change.

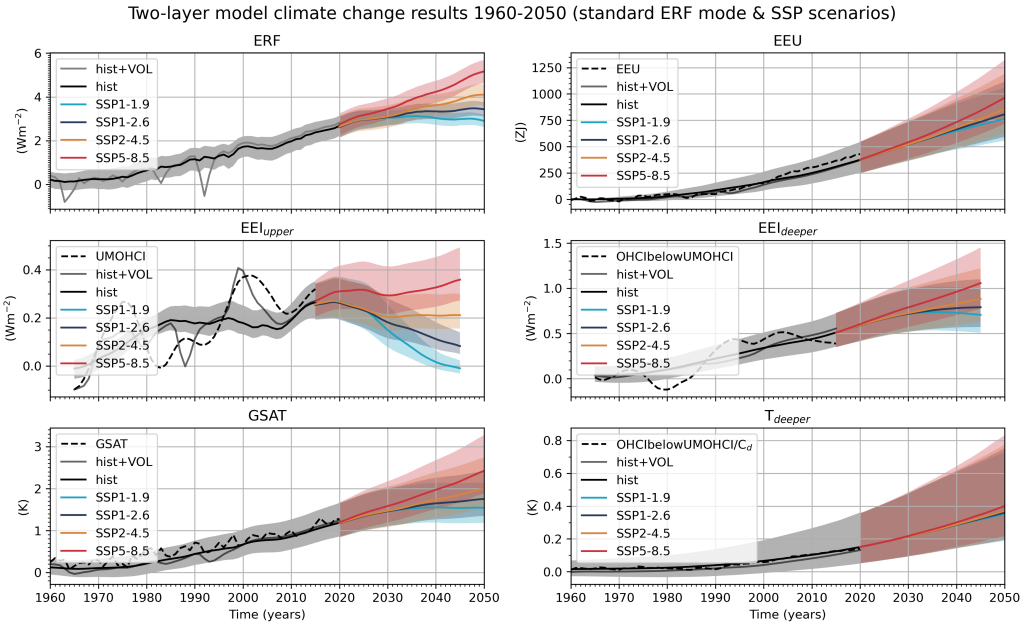


Figure 6.4: Two-layer model climate change results 1960-2050 with prescribed forcing, observation-based until 2020 and SSP scenario-based forcing up to 2050 including 90% CI corridors. The results from using historical data excluding volcanic forcing for the model are shown as hist and using time-dependent volcanic forcing as hist+VOL. Scenarios are denoted as SSP with number and the respective approximate radiative forcing in the year 2100 in W m^{-2} after a dash. The used Effective Radiative Forcing (ERF) is shown in the upper left panel, Earth Energy Uptake (EEU) in the upper right. The two components of the EEI for the upper and deeper layer are seen in the middle. The bottom row shows the two most important outputs, the surface-layer (GSAT) and deeper-layer (T_{deeper}) temperatures.

7 Conclusion

This work has presented a detailed account of energy balance at the Top of the Atmosphere (TOA). Effective Radiative Forcing (ERF) from all climate forcings has been assessed. Natural forcings including solar and volcanic contributions are shown to be zero in the multi-decadal mean. Greenhouse gas forcings have been shown to make up the largest part of radiative forcing and their rise is leading to increased heat storage in the Earth system. Other climate forcings from short-term climate forcers and minor gases have been shown to be less relevant. The aerosol forcing dataset used in this study constitutes a large improvement in uncertainties related to earlier estimates before the IPCC 2021 report (Smith et al. 2021b).

Earth Energy Imbalance (EEI) has been calculated on decadal timescales, with an uncertainty derived from Earth Energy Uptake (EEU). This approach has led to a better-constrained uncertainty than in previous assessments. OHC uncertainty from two datasets with associated uncertainties have been combined, yielding a tighter uncertainty for the total ocean. Atmospheric heat content increase rate data from up-to-date calculations with small uncertainties have helped to improve the atmospheric component. Though this change is small in absolute terms, it has recently increased particularly strong in relative terms. Cryosphere and land data were taken from previous work.

For Global Surface Air Temperature (GSAT) the HadCRUT5 dataset has been shown to incorporate an uncertainty model suitable for a robust estimate of the climate feedback parameter α_{FP}.

This study found $\alpha_{FP} = 1.4 \pm 0.4\,\mathrm{W\,m^{-2}\,K^{-1}}$, compared to $\alpha_{FP} = 1.3 \pm 0.7\,\mathrm{W\,m^{-2}}$ from a recent comprehensive process-based assessment by the review Sherwood et al. (2020). This energy balance estimate is closer to process-based assessment results than other estimates shown in Forster (2016).

Finally, a simple two-layer energy balance model was used to obtain results for GSAT, EEU and EEI under historical forcings and climate change scenarios. It has been found to produce reasonable GSAT and EEI that agree well with observational data and is also found suitable for calculating α_{FP}. The standard ERF mode is best for this purpose, although prescribing decadal temperature and calculating the results in reverse also produces satisfactory results.

The future Shared Socioeconomic Pathway (SSP) scenarios that incorporate climate mitigation, have been found to give decreasing EEI up to 2050, whereas the fossil-fuel development scenario shows rising EEI until 2050. Only under the most sustainable scenario the uppermost ocean-layer contribution to EEI reaches zero near 2050. This is when the deeper oceans may begin to act as a heat source, again starting to keep the surface layer warm.

List of Figures

2.1 The global energy budget (Wild et al. 2014) 5

3.1 Effects of anthropogenic aerosols on the radiation budget including aerosol-cloud and aerosol-radiation interactions (Bellouin et al. 2020) 12

4.1 Earth energy uptake (EEU) since 1960 21
4.2 Effecticve radiative forcing (ERF) 23
4.3 Global Surface Air Temperature (GSAT) from HadCRUT5 (Morice et al. 2021), ERA-5 (Hersbach et al. 2020) and GISTEMP (Lenssen et al. 2019) 24
4.4 Decadal-mean Earth Energy Imbalance (EEI) and heat content/ energy uptake increase rates in all subsystems of the climate system 25
4.5 Forcing-Response-Imbalance estimates 27
4.6 Comparison of TMOHC (0-100 m), UMOHC (0-300 m) and the bottom upper-ocean OHC at 300-700 m from IAP data and ORAS5 data 28
4.7 Sum of decadal-mean topmost (TM) and uppermost (UM) ocean with atmospheric (AHC) heat content increase compared to GSAT (T_s) increase with time 29

5.1 Climate feedback parameter α_{FP} estimates inferred from energy balance 35

6.1 Two-layer model results 1960-2020 (standard ERF mode) 38
6.2 Two-layer model results 1960-2020 with prescribed GSAT (Preset GSAT mode) 39
6.3 Two-layer model results 1960-2020 with prescribed EEI (Preset EEI mode) 41
6.4 Two-layer model climate change results 1960-2050 with prescribed forcing, including SSP scenarios up to 2050 42

List of Tables

3.1 Parameters for calculating ERF of major GHGs (from Meinshausen et al. 2020) 11
3.2 Two layer emulator parameters after (Smith et al. 2021a) 16

Bibliography

Bellouin, N., J. Quaas, E. Gryspeerdt, S. Kinne, P. Stier, D. Watson-Parris, O. Boucher, K. S. Carslaw, M. Christensen, A.-L. Daniau, J.-L. Dufresne, G. Feingold, S. Fiedler, P. Forster, A. Gettelman, J. M. Haywood, U. Lohmann, F. Malavelle, T. Mauritsen, D. T. McCoy, G. Myhre, J. Mülmenstädt, D. Neubauer, A. Possner, M. Rugenstein, Y. Sato, M. Schulz, S. E. Schwartz, O. Sourdeval, T. Storelvmo, V. Toll, D. Winker, and B. Stevens (2020). "Bounding Global Aerosol Radiative Forcing of Climate Change". *Reviews of Geophysics* 58.1. DOI: 10.1029/2019rg000660.

Butler, J. H. and S. A. Montzka (2021). "The NOAA Annual Greenhouse Gas Index (AGGI) 2020". *http://www.esrl.noaa.gov/gmd/aggi/aggi.html*. URL: http://www.esrl.noaa.gov/gmd/aggi/aggi.html.

Cheng, L., J. Abraham, K. E. Trenberth, J. Fasullo, T. Boyer, R. Locarnini, B. Zhang, F. Yu, L. Wan, X. Chen, X. Song, Y. Liu, M. E. Mann, F. Reseghetti, S. Simoncelli, V. Gouretski, G. Chen, A. Mishonov, J. Reagan, and J. Zhu (2021). "Upper Ocean Temperatures Hit Record High in 2020". *Advances in Atmospheric Sciences* 38.4, pp. 523–530. DOI: 10.1007/s00376-021-0447-x.

Cheng, L. and J. Zhu (2016). "Benefits of CMIP5 Multimodel Ensemble in Reconstructing Historical Ocean Subsurface Temperature Variations". *Journal of Climate* 29.15, pp. 5393–5416. DOI: 10.1175/jcli-d-15-0730.1.

Coddington, O., J. L. Lean, D. Lindholm, P. Pilewskie, M. Snow, and NOAA CDR Program (2015). *NOAA Climate Data Record (CDR) of Total Solar Irradiance (TSI), NRLTSI Version 2*. DOI: 10.7289/V55B00C1.

Cuesta-Valero, F. J., A. Garcıa-Garcıa, H. Beltrami, J. F. González-Rouco, and E. Garcıa-Bustamante (2021). "Long-term global ground heat flux and continental heat storage from geothermal data". *Climate of the Past* 17.1, pp. 451–468. DOI: 10.5194/cp-17-451-2021.

Dong, Y., K. C. Armour, M. D. Zelinka, C. Proistosescu, D. S. Battisti, C. Zhou, and T. Andrews (2020). "Intermodel Spread in the Pattern Effect and Its Contribution to Climate Sensitivity in CMIP5 and CMIP6 Models". *Journal of Climate* 33.18, pp. 7755–7775. DOI: 10.1175/jcli-d-19-1011.1.

Eyring, V., S. Bony, G. A. Meehl, C. A. Senior, B. Stevens, R. J. Stouffer, and K. E. Taylor (2016). "Overview of the Coupled Model Intercomparison Project Phase 6 (CMIP6) experimental design and organization". *Geoscientific Model Development* 9.5, pp. 1937–1958. DOI: 10.5194/gmd-9-1937-2016.

Forster, P., T. Storelvmo, K. Armour, W. Collins, J.-L. Dufresne, D. Frame, D. Lunt, T. Mauritsen, M. Palmer, M. Watanabe, M. Wild, and H. Zhang (2021). "The Earth's Energy Budget, Climate Feedbacks, and Climate Sensitivity". In:

Climate Change 2021: The Physical Science Basis. Contribution of Working Group I to the Sixth Assessment Report of the Intergovernmental Panel on Climate Change. Ed. by V. M. Delmotte, P. Zhai, A. Pirani, S. L. Connors, C. Péan, S. Berger, N. Caud, Y. Chen, L. Goldfarb, M. I. Gomis, M. Huang, K. Leitzell, E. Lonnoy, J. B. R. Matthews, T. K. Maycock, T. Waterfield, O. Yelekçi, R. Yu, and B. Zhou. Cambridge University Press.

Forster, P. M. (2016). "Inference of Climate Sensitivity from Analysis of Earth's Energy Budget". *Annual Review of Earth and Planetary Sciences* 44.1, pp. 85–106. DOI: 10.1146/annurev-earth-060614-105156.

Gelaro, R., W. McCarty, M. J. Suárez, R. Todling, A. Molod, L. Takacs, C. A. Randles, A. Darmenov, M. G. Bosilovich, R. Reichle, K. Wargan, L. Coy, R. Cullather, C. Draper, S. Akella, V. Buchard, A. Conaty, A. M. da Silva, W. Gu, G.-K. Kim, R. Koster, R. Lucchesi, D. Merkova, J. E. Nielsen, G. Partyka, S. Pawson, W. Putman, M. Rienecker, S. D. Schubert, M. Sienkiewicz, and B. Zhao (2017). "The Modern-Era Retrospective Analysis for Research and Applications, Version 2 (MERRA-2)". *Journal of Climate* 30.14, pp. 5419–5454. DOI: 10.1175/jcli-d-16-0758.1.

Geoffroy, O., D. Saint-Martin, G. Bellon, A. Voldoire, D. J. L. Olivié, and S. Tytéca (2013a). "Transient Climate Response in a Two-Layer Energy-Balance Model. Part II: Representation of the Efficacy of Deep-Ocean Heat Uptake and Validation for CMIP5 AOGCMs". *Journal of Climate* 26.6, pp. 1859–1876. DOI: 10.1175/jcli-d-12-00196.1.

Geoffroy, O., D. Saint-Martin, D. J. L. Olivié, A. Voldoire, G. Bellon, and S. Tytéca (2013b). "Transient Climate Response in a Two-Layer Energy-Balance Model. Part I: Analytical Solution and Parameter Calibration Using CMIP5 AOGCM Experiments". *Journal of Climate* 26.6, pp. 1841–1857. DOI: 10.1175/jcli-d-12-00195.1.

Ghimire, B., C. A. Williams, J. Masek, F. Gao, Z. Wang, C. Schaaf, and T. He (2014). "Global albedo change and radiative cooling from anthropogenic land cover change, 1700 to 2005 based on MODIS, land use harmonization, radiative kernels, and reanalysis". *Geophysical Research Letters* 41.24, pp. 9087–9096. DOI: 10.1002/2014gl061671.

GISTEMP Team (2021). *GISS Surface Temperature Analysis (GISTEMP), version 4. NASA Goddard Institute for Space Studies*. Dataset accessed 2021-07-01 at data.giss.nasa.gov/gistemp/.

Gorfer, M. (2022). "Monitoring of climate change and variability in atmospheric heat content based on climate records and reanalyses". In: Wegener Center Scientific Report 94-2022. University of Graz. Wegener Center Verlag. ISBN: 978-3-9504700-3-1.

Gregory, J. M., R. J. Stouffer, S. C. B. Raper, P. A. Stott, and N. A. Rayner (2002). "An Observationally Based Estimate of the Climate Sensitivity". *Journal of Climate* 15.22, pp. 3117–3121. DOI: 10.1175/1520-0442(2002)015<3117:aobeot>2.0.co;2.

Gulev, S. K., P. W. Thorne, J. Ahn, F. J. Dentener, C. Domingues, S. Gerland, D. Gong, D. S. Kaufman, H. Nnamchi, J. Quaas, J. A. Rivera, S. Sathyendranath, S. L. Smith, B. Trewin, K. von Schuckmann, and R. S. Vose (2021). "Changing State of the Climate System". In: *Climate Change 2021: The Physical Science Basis. Contribution of Working Group I to the Sixth Assessment Report of the Intergovernmental Panel on Climate Change*. Ed. by V. M. Delmotte, P. Zhai, A. Pirani, S. L. Connors, C. Péan, S. Berger, N. Caud, Y. Chen, L. Goldfarb, M. I. Gomis, M. Huang, K. Leitzell, E. Lonnoy, J. B. R. Matthews, T. K. Maycock, T. Waterfield, O. Yelekçi, R. Yu, and B. Zhou. Cambridge University Press.

Hansen, J., M. Sato, P. Kharecha, and K. von Schuckmann (2011). "Earth's energy imbalance and implications". *Atmospheric Chemistry and Physics* 11.24, pp. 13421–13449. DOI: 10.5194/acp-11-13421-2011.

Hersbach, H. et al. (2020). "The ERA5 global reanalysis". *Quarterly Journal of the Royal Meteorological Society* 146.730, pp. 1999–2049. DOI: 10.1002/qj.3803.

Hoesly, R. M., S. J. Smith, L. Feng, Z. Klimont, G. Janssens-Maenhout, T. Pitkanen, J. J. Seibert, L. Vu, R. J. Andres, R. M. Bolt, T. C. Bond, L. Dawidowski, N. Kholod, J.-i. Kurokawa, M. Li, L. Liu, Z. Lu, M. C. P. Moura, P. R. O'Rourke, and Q. Zhang (2018). "Historical (1750–2014) anthropogenic emissions of reactive gases and aerosols from the Community Emissions Data System (CEDS)". *Geoscientific Model Development* 11.1, pp. 369–408. DOI: 10.5194/gmd-11-369-2018.

Jiménez-de-la-Cuesta, D. and T. Mauritsen (2019). "Emergent constraints on Earth's transient and equilibrium response to doubled CO2 from post-1970s global warming". *Nature Geoscience* 12.11, pp. 902–905. DOI: 10.1038/s41561-019-0463-y.

Kirchengast, G., D. Kohlfürst, and G. Thalassinos (2021). "Graz Climate Change Indicators including Tracking of Earth's Energy Imbalance and related Radiative Forcing and Response". In: *Presented at AGU Fall Meeting 2021*.

Kirchengast, G., F. Ladstädter, A. Steiner, M. Gorfer, F. Lippl, and B. Angerer (2019). "Climate Trends and Variability in Atmosphere Heat Content and Atmosphere-Ocean Heat Exchanges: Space Geodesy is Key". In: *IUUG 2019 Conf. Inv. Pres. Montreal CA*.

Kobayashi, S., Y. Ota, Y. Harada, A. Ebita, M. Moriya, H. Onoda, K. Onogi, H. Kamahori, C. Kobayashi, H. Endo, K. Miyaoka, and K. Takahashi (2015). "The JRA-55 Reanalysis: General Specifications and Basic Characteristics". *Journal of the Meteorological Society of Japan. Ser. II* 93.1, pp. 5–48. DOI: 10.2151/jmsj.2015-001.

Kovilakam, M., L. W. Thomason, N. Ernest, L. Rieger, A. Bourassa, and L. Millán (2020). "The Global Space-based Stratospheric Aerosol Climatology (version 2.0): 1979–2018". *Earth System Science Data* 12.4, pp. 2607–2634. DOI: 10.5194/essd-12-2607-2020.

Larson, E. J. L. and R. W. Portmann (2016). "A Temporal Kernel Method to Compute Effective Radiative Forcing in CMIP5 Transient Simulations∗". *Journal of Climate* 29.4, pp. 1497–1509. DOI: 10.1175/jcli-d-15-0577.1.

Lee, D., D. Fahey, A. Skowron, M. Allen, U. Burkhardt, Q. Chen, S. Doherty, S. Freeman, P. Forster, J. Fuglestvedt, A. Gettelman, R. D. León, L. Lim, M. Lund, R. Millar, B. Owen, J. Penner, G. Pitari, M. Prather, R. Sausen, and L. Wilcox (2021). "The contribution of global aviation to anthropogenic climate forcing for 2000 to 2018". *Atmospheric Environment* 244, p. 117834. DOI: 10.1016/j.atmosenv.2020.117834.

Lenssen, N. J. L., G. A. Schmidt, J. E. Hansen, M. J. Menne, A. Persin, R. Ruedy, and D. Zyss (2019). "Improvements in the GISTEMP Uncertainty Model". *Journal of Geophysical Research: Atmospheres* 124.12, pp. 6307–6326. DOI: 10.1029/2018jd029522.

Liu, R., H. Su, K.-N. Liou, J. H. Jiang, Y. Gu, S. C. Liu, and C.-J. Shiu (2018). "An Assessment of Tropospheric Water Vapor Feedback Using Radiative Kernels". *Journal of Geophysical Research: Atmospheres* 123.3, pp. 1499–1509. DOI: 10.1002/2017jd027512.

Loeb, N. G., G. C. Johnson, T. J. Thorsen, J. M. Lyman, F. G. Rose, and S. Kato (2021). "Satellite and Ocean Data Reveal Marked Increase in Earth's Heating Rate". *Geophysical Research Letters* 48.13. DOI: 10.1029/2021gl093047.

Lund, M. T., G. Myhre, and B. H. Samset (2019). "Anthropogenic aerosol forcing under the Shared Socioeconomic Pathways". *Atmospheric Chemistry and Physics* 19.22, pp. 13827–13839. DOI: 10.5194/acp-19-13827-2019.

Luo, B. (2018). *Release Notes Stratospheric Aerosol Radiative Forcing and SAD version v4.0.0 1850 - 2016*. (last access: 1 April 2021).

Meinshausen, M., Z. R. J. Nicholls, J. Lewis, M. J. Gidden, E. Vogel, M. Freund, U. Beyerle, C. Gessner, A. Nauels, N. Bauer, J. G. Canadell, J. S. Daniel, A. John, P. B. Krummel, G. Luderer, N. Meinshausen, S. A. Montzka, P. J. Rayner, S. Reimann, S. J. Smith, M. van den Berg, G. J. M. Velders, M. K. Vollmer, and R. H. J. Wang (2020). "The shared socio-economic pathway (SSP) greenhouse gas concentrations and their extensions to 2500". *Geoscientific Model Development* 13.8, pp. 3571–3605. DOI: 10.5194/gmd-13-3571-2020.

Meinshausen, M., E. Vogel, A. Nauels, K. Lorbacher, N. Meinshausen, D. M. Etheridge, P. J. Fraser, S. A. Montzka, P. J. Rayner, C. M. Trudinger, P. B. Krummel, U. Beyerle, J. G. Canadell, J. S. Daniel, I. G. Enting, R. M. Law, C. R. Lunder, S. O'Doherty, R. G. Prinn, S. Reimann, M. Rubino, G. J. M. Velders, M. K. Vollmer, R. H. J. Wang, and R. Weiss (2017). "Historical greenhouse gas concentrations for climate modelling (CMIP6)". *Geoscientific Model Development* 10.5, pp. 2057–2116. DOI: 10.5194/gmd-10-2057-2017.

Morice, C. P., J. J. Kennedy, N. A. Rayner, J. P. Winn, E. Hogan, R. E. Killick, R. J. H. Dunn, T. J. Osborn, P. D. Jones, and I. R. Simpson (2021). "An Updated Assessment of Near-Surface Temperature Change From 1850: The HadCRUT5 Data Set". *Journal of Geophysical Research: Atmospheres* 126.3. DOI: 10.1029/2019jd032361.

Otto, A., F. E. L. Otto, O. Boucher, J. Church, G. Hegerl, P. M. Forster, N. P. Gillett, J. Gregory, G. C. Johnson, R. Knutti, N. Lewis, U. Lohmann, J. Marotzke, G. Myhre, D. Shindell, B. Stevens, and M. R. Allen (2013). "Energy budget

constraints on climate response". *Nature Geoscience* 6.6, pp. 415–416. DOI: 10.1038/ngeo1836.

Roemmich, D. et al. (2019). "On the Future of Argo: A Global, Full-Depth, Multi-Disciplinary Array". *Frontiers in Marine Science* 6. DOI: 10.3389/fmars.2019.00439.

Schuckmann, K. von, L. Cheng, M. D. Palmer, J. Hansen, C. Tassone, V. Aich, S. Adusumilli, H. Beltrami, T. Boyer, F. J. Cuesta-Valero, D. Desbruyères, C. Domingues, A. Garcıa-Garcıa, P. Gentine, J. Gilson, M. Gorfer, L. Haimberger, M. Ishii, G. C. Johnson, R. Killick, B. A. King, G. Kirchengast, N. Kolodziejczyk, J. Lyman, B. Marzeion, M. Mayer, M. Monier, D. P. Monselesan, S. Purkey, D. Roemmich, A. Schweiger, S. I. Seneviratne, A. Shepherd, D. A. Slater, A. K. Steiner, F. Straneo, M.-L. Timmermans, and S. E. Wijffels (2020). "Heat stored in the Earth system: where does the energy go?" *Earth System Science Data* 12.3, pp. 2013–2041. DOI: 10.5194/essd-12-2013-2020.

Schwartz, S. E. (2012). "Determination of Earth's Transient and Equilibrium Climate Sensitivities from Observations Over the Twentieth Century: Strong Dependence on Assumed Forcing". *Surveys in Geophysics* 33.3-4, pp. 745–777. DOI: 10.1007/s10712-012-9180-4.

Sherwood, S. C., M. J. Webb, J. D. Annan, K. C. Armour, P. M. Forster, J. C. Hargreaves, G. Hegerl, S. A. Klein, K. D. Marvel, E. J. Rohling, M. Watanabe, T. Andrews, P. Braconnot, C. S. Bretherton, G. L. Foster, Z. Hausfather, A. S. Heydt, R. Knutti, T. Mauritsen, J. R. Norris, C. Proistosescu, M. Rugenstein, G. A. Schmidt, K. B. Tokarska, and M. D. Zelinka (2020). "An Assessment of Earth's Climate Sensitivity Using Multiple Lines of Evidence". *Reviews of Geophysics* 58.4. DOI: 10.1029/2019rg000678.

Skeie, R. B., G. Myhre, Ø. Hodnebrog, P. J. Cameron-Smith, M. Deushi, M. I. Hegglin, L. W. Horowitz, R. J. Kramer, M. Michou, M. J. Mills, D. J. L. Olivié, F. M. O. Connor, D. Paynter, B. H. Samset, A. Sellar, D. Shindell, T. Takemura, S. Tilmes, and T. Wu (2020). "Historical total ozone radiative forcing derived from CMIP6 simulations". *NPJ Climate and Atmospheric Science* 3.1, pp. 1–10. DOI: 10.1038/s41612-020-00131-0.

Slater, T., I. R. Lawrence, I. N. Otosaka, A. Shepherd, N. Gourmelen, L. Jakob, P. Tepes, L. Gilbert, and P. Nienow (2021). "Earth's ice imbalance". *The Cryosphere* 15.1, pp. 233–246. DOI: 10.5194/tc-15-233-2021.

Smith, C., Z. R. J. Nicholls, K. Armour, W. Collins, P. Forster, M. Meinshausen, M. Palmer, and M. Watanabe (2021a). "The Earth's Energy Budget, Climate Feedbacks, and Climate Sensitivity Supplementary Material". In: *Climate Change 2021: The Physical Science Basis. Contribution of Working Group I to the Sixth Assessment Report of the Intergovernmental Panel on Climate Change*. Ed. by V. M. Delmotte, P. Zhai, A. Pirani, S. L. Connors, C. Péan, S. Berger, N. Caud, Y. Chen, L. Goldfarb, M. I. Gomis, M. Huang, K. Leitzell, E. Lonnoy, J. B. R. Matthews, T. K. Maycock, T. Waterfield, O. Yelekçi, R. Yu, and B. Zhou. Cambridge University Press. URL: ipcc.ch.

Smith, C. J., G. R. Harris, M. D. Palmer, N. Bellouin, W. Collins, G. Myhre, M. Schulz, J.-C. Golaz, M. Ringer, T. Storelvmo, and P. M. Forster (2021b). "Energy Budget Constraints on the Time History of Aerosol Forcing and Climate Sensitivity". *Journal of Geophysical Research: Atmospheres* 126.13. DOI: 10.1029/2020jd033622.

Steffen, W., K. Richardson, J. Rockström, S. E. Cornell, I. Fetzer, E. M. Bennett, R. Biggs, S. R. Carpenter, W. de Vries, C. A. de Wit, C. Folke, D. Gerten, J. Heinke, G. M. Mace, L. M. Persson, V. Ramanathan, B. Reyers, and S. Sörlin (Feb. 2015). "Planetary boundaries: Guiding human development on a changing planet". *Science* 347.6223. DOI: 10.1126/science.1259855.

Twomey, S. (1977). "The Influence of Pollution on the Shortwave Albedo of Clouds". *Journal of the Atmospheric Sciences* 34.7, pp. 1149–1152. DOI: 10.1175/1520-0469(1977)034<1149:tiopot>2.0.co;2.

Wild, M. (2017). "Towards Global Estimates of the Surface Energy Budget". *Current Climate Change Reports* 3.1, pp. 87–97. DOI: 10.1007/s40641-017-0058-x.

Wild, M., D. Folini, M. Z. Hakuba, C. Schär, S. I. Seneviratne, S. Kato, D. Rutan, C. Ammann, E. F. Wood, and G. König-Langlo (2014). "The energy balance over land and oceans: an assessment based on direct observations and CMIP5 climate models". *Climate Dynamics* 44.11-12, pp. 3393–3429. DOI: 10.1007/s00382-014-2430-z.

Yeo, K. L., N. A. Krivova, and S. K. Solanki (2017). "EMPIRE: A robust empirical reconstruction of solar irradiance variability". *Journal of Geophysical Research: Space Physics* 122.4, pp. 3888–3914. DOI: 10.1002/2016ja023733.

Zuo, H., M. A. Balmaseda, S. Tietsche, K. Mogensen, and M. Mayer (2019). "The ECMWF operational ensemble reanalysis–analysis system for ocean and sea ice: a description of the system and assessment". *Ocean Science* 15.3, pp. 779–808. DOI: 10.5194/os-15-779-2019.

Anthropogenic climate warming caused by greenhouse gas emissions has led to a positive imbalance in the energy budget of the Earth. The Earth Energy Imbalance (EEI) represents the rate of change in heat stored by the climate system in response to global warming and thus the portion of forcing the climate has not yet responded to. This study uses observations for Earth energy uptake (EEU) from 1960 to 2020 in all subsystems of the Earth system, comprising heat energy fluxes into oceans, atmosphere, land, and cryosphere. With the help of uncertainty estimates for energy uptake, EEI is assessed as a decadal-mean rate of change. The decadalmean EEI has not only been maintained, but also increased in recent decades. Combining it with observations of effective radiative forcing (ERF) and global surface air temperature (GSAT), an energy-budget derived estimate of the climate feedback parameter of 1.4 Wm^{-2} K^{-1} with an uncertainty of 0.4 Wm^{-2} K^{-1} is achieved. These three variables have also been used as input parameters for a simple two-layer energy balance model used to study historical and scenario-based development of the GSAT, EEI, ERF and the climate feedback parameter. The model produced satisfactory results that agree well with observations. By using the model in alternative modes, i.e., different variables as input, it can be seen that GSAT records agree well with ERF in the decadal mean. Hope for mitigating climate warming can be drawn from using this simple model under climate change scenarios. Assuming a sustainable future, the uppermost ocean-layer component of the EEI could reach zero already near 2050. This might lead to the deeper oceans starting to act as a heat source from beneath.

Die anthropogene Klimaerwärmung durch Treibhausgasemissionen hat zu einem Ungleichgewicht (Imbalance) im Energiehaushalt der Erde geführt. Diese Earth Energy Imbalance (EEI) stellt die Änderungsrate derWärme dar, die vom Klimasystem als Reaktion auf die globale Erwärmung gespeichert wird, und somit den Teil, auf den das Klima noch nicht reagiert hat. Diese Studie verwendet Beobachtungen zur Earth Energy Uptake (EEU) von 1960 bis 2020 in allen Subsystemen des Erdsystems, einschließlich der Wärmeenergieflüsse in Ozeane, Atmosphäre, Land und Kryosphäre. Mithilfe von Unsicherheitsschätzungen für die Energieaufnahme wird EEI als dekadische mittlere Änderungsrate untersucht. Die dekadisch gemittelte EEI wurde in den letzten Jahrzehnten nicht nur gehalten, sondern nahm weiter zu. Kombiniert mit Beobachtungen des effektiven Strahlungsantriebs (ERF) und der globalen Oberflächenlufttemperatur (GSAT), ergibt sich eine vom Energiebudget abgeleiteten Schätzung des Klimarückkopplungsparameters von 1,4 Wm^{-2} K^{-1} mit einer Unsicherheit von 0,4 Wm^{-2} K^{-1}. Diese drei Variablen wurden auch als Eingabeparameter für ein einfaches zweischichtiges Energiebilanzmodell verwendet, um die historische und szenariobasierte Entwicklung von GSAT, EEI, ERF und des Klimarückkopplungsparameters zu untersuchen. Das Modell lieferte zufriedenstellende Ergebnisse, die gut mit den Beobachtungen übereinstimmen. Durch die Verwendung des Modells in alternativen Modi, d. h. verschiedenen Variablen als Eingabe, ist ersichtlich, dass GSAT-Datensätze im dekadischen Mittel gut mit ERF übereinstimmen. Aus der Verwendung dieses einfachen Modells in Klimawandelszenarien kann Hoffnung auf eine Eindämmung der Klimaerwärmung geschöpft werden. Geht man von einer nachhaltigen Zukunft aus, könnte die Komponente der obersten Ozeanschicht des EEI bereits um das Jahr 2050 Null erreichen. Dies könnte dazu führen, dass die tieferen Ozeane beginnen, als Wärmequelle von unten zu fungieren.

SR 97 | 2023 Tracking global warming based on Earth energy uptake and energy imbalance modeling
Wegener Center Verlag, University of Graz, Austria. ISBN 978-3-9504700-6-2